Water infiltration and deformation within the uppermost mantle along the Marion transform fault, Southwest Indian Ridge

（南西インド洋海嶺 **Marion transform** 断層における最上部マントルへの水の浸透と変形）

KAKIHATA Yuki
柿畑　優季

Department of Earth and Planetary Sciences
Graduate School of Environmental Studies
Nagoya University

Mar. 2023

CONTENTS

Part 1

Part 2

Overview

Transform faults are offsets along oceanic ridges with a length of 30 km or more, dividing ridge axes into segments, some of which reach 1000 km. These offsets are strike-slip faults where oceanic plates formed at ridges pass, and unlike other strike-slip faults, the direction of fault motion depends on the direction of plate movement because of seafloor spreading. Transform faults form steep valley topography and cliffs, and the valley is the deepest near the intersection with the ridge axis. Most transform faults connect ridge to ridge, however there are small numbers of transform faults that connect ridge to trench and trench to trench.

The viscosity of peridotite, the main component of the upper mantle, is decreased significantly by water, and transform faults could be water inlets to the uppermost mantle. Therefore, water infiltration and deformation of peridotite beneath transform faults are important to understand the driving force of plate tectonics.

Of the oceanic ridges, those with particularly slow spreading rate of <20 mm/y are called ultraslow-spreading ridges. Under the ultraslow-spreading ridges, only a small amount of magma would be supplied from the deeper part, so that the influence of cooling should be relatively large. Therefore, magma chambers and melt could not exist stably. As a result, since the production of oceanic crust is unstable, mantle peridotites could have been exposed on the seafloor.

The Southwest Indian Ridge (SWIR) is an ultraslow-spreading ridge, and average thickness of oceanic crust is very thin (1~2 km) due to inactive volcanic activities. Thus, peridotites have been collected from the transform faults and fracture zones along the SWIR by multiple dredge surveys.

Deformed textures and crystallographic preferred orientations (CPOs) of olivine, which are developed by plastic deformation of peridotite, provide clues to constrain the deformation condition. Furthermore, it is known that olivine crystal has seismic anisotropy, and if crystal orientations of olivine are concentrated in a specific direction, peridotites itself has distinct seismic anisotropies. The CPOs and seismic anisotropies are good indices to characterize deformation of peridotites. Additionally, inclusions in minerals are one of the clues for material cycle, and their compositions can clarify not only temperature and pressure conditions when they were formed but also spatial distribution of elements that have penetrated into minerals. However, there are few studies for deformed textures and CPOs of peridotites and inclusions related to water infiltration, thus deformation of mantle peridotites and material cycle around transform fault have been ambiguous.

In this PhD study, I studied 14 peridotites derived from Marion transform fault, SWIR from the aspects of deformation, chemical composition and inclusion. I performed textural analyses by optical microscope and electron backscattered diffraction (EBSD) to understand the types of deformation (i.e., strength, conditions and mechanisms). Raman spectroscopy and electron microprobe microanalysis (EPMA) were performed to understand the chemical properties and reactions of melt with mantle peridotites. A series of studies show that water seems to infiltrate into shallow upper mantle from transform fault and affects deformation of mantle peridotites beneath the transform fault.

Part 1

Transform fault extended into a shear zone from the seafloor, so that rocks are deformed under hydrous condition even at depth. Structural and petrological studies focusing on crystallographic preferred orientations (CPOs) of constituent minerals can produce several clues to reveal deformation conditions and mechanisms beneath the transform fault. However, most of the studies on transform faults have paid attention to chemical compositions, and there are few studies focusing on structures of the rocks. Therefore, the effects of water on shear deformation beneath transform faults are not well understood. In Part 1, I studied 7 peridotites by optical microscope and EBSD, and found olivine CPOs developed under hydrous conditions in the peridotites with plastically deformed amphiboles. Based on the CPOs and deformed amphibole, I concluded that mantle peridotites beneath the transform fault was deformed under hydrous conditions.

Part 2

Evidence of water infiltration along transform faults includes hydrous inclusions in addition to hydrous minerals and olivine CPOs developed under hydrous condition. Fluid inclusions have been actually found in peridotites derived from transform faults. In Part 2, I found numerous inclusions in coarse olivine grains, and analyzed them by Raman spectroscopy. The inclusions exhibited various shapes, and consisted of low-temperature serpentine, hydrogen, methane and graphite. Hydrogen, methane and graphite are generated related to serpentinization, and they need water to form. Therefore, it is suggested that water infiltrated into upper mantle and was trapped as inclusions in olivine grains, and reacted with host olivine, then hydrogen and methane were generated, finally carbon dioxide and a part of the methane were consumed to generate graphite.

Part 1

Water infiltration and hydrous shearing of mantle beneath a transform fault: Marion transform fault, Southwest Indian Ridge

ABSTRACT

The ultraslow spreading (14 mm/yr) Southwest Indian Ridge lies between the Bouvet and Rodriguez Triple Junctions extending from 1°W to 70°E. I studied the microstructural development of 7 peridotite samples obtained from Marion transform fault of Southwest Indian Ridge by the PROTEA Expedition Leg 5 cruise in 1983 of the RV Melville. The peridotites consist of olivine, orthopyroxene and clinopyroxene with minor amounts of amphibole, plagioclase and chlorite, as well as secondary minerals such as serpentine and magnetite. The peridotites were classified into two groups based on their microstructures: 2 ultramylonites, mostly consisting of extremely fine grains (3-5μm), and 5 heterogeneous tectonites consisting of deformed coarse-granular textures and subsequently developed fine-grained shear zones. Olivine Mg# [=Mg/(Mg+Fe)] is 0.895-0.912 and spinel Cr# [=Cr/(Cr+Al) atomic ratio] is 0.171-0.339, indicating very fertile to moderately depleted mantle compositions. Amphibole grains have the chemical compositions of tremolite and magnesio-hornblende. The ultramylonites have intensely deformed amphibole grains, whereas the tectonites have amphibole ranging from undeformed grains to highly deformed grains, indicating that amphibole formed before and/or during intense shearing in mantle. Moreover, extremely fine grain sizes of olivine and brittle microstructures in both pyroxene and spinel grains such as micro-boudins suggest that these peridotites have been sheared under high stress conditions. Olivine crystal-fabrics within the deformed amphibole bearing peridotites have B and E types developed under hydrous conditions, whereas olivine fabrics within the undeformed amphibole bearing peridotites have A and D types developed under anhydrous conditions. Consequently, the petrophysical characteristics of peridotites in this study indicate that the uppermost mantle below the Marion transform fault has been locally but intensely hydrated during shearing due to deep rooted detachment faulting at the inside-corner high adjacent to the transform.

1. INTRODUCTION

Water decreases viscosity of peridotite by several orders of magnitude (Karato and Jung, 2003). Plate tectonics requires low viscosity of mantle, so that infiltration of water into mantle plays an important role for occurrence of plate tectonics (Korenaga, 2007, 2010, 2013). There are several places where faults and fractures reach to upper mantle on the Earth, and water enters the Earth's interior (Kerric, 2002). For example, water is thought to go into mantle due to thermal cracking near a ridge (Korenaga, 2007, 2010), carried down in subduction zones (e.g., Ulmer and Trommsdorff, 1995; Liu et al., 1996), during flexure at an outer rise (e.g., Peacock, 2001; Hatakeyama et al., 2017) and due to serpentinization at transform faults (Francis, 1981; Roland et al., 2010).

Several studies proposed that fracture zones are connected to the origin of the subduction zones (Mueller and Phillips, 1991; Hall et al., 2003; Stern, 2004; Hirauchi et al., 2016). Mueller and Phillips (1991) and Hall et al. (2003) showed that differences in densities of the passing plates resulted in the initiation of subduction at a fracture zone. However, recent studies suggested that a weak crust (coefficient of friction: $\mu<0.1$) would be required for the initiation of subduction (Stern, 2004; Hirauchi et al., 2016). Thus, the occurrence of hydrous minerals such as amphibole and chlorite in abyssal peridotite mylonites from the walls of transform valleys are of great interest due to the potential of hydrolytic weakening of the transform slip zone at high temperatures in the lithosphere (e.g., Jaroslow et al., 1996; Stern, 2004; Warren and Hirth, 2006; Kohli and Warren, 2020; Prigent et al., 2020; Kakihata et al., 2022) with important potential implications for plate tectonics.

Olivine crystallographic preferred orientations (CPOs) in peridotites can be used as an approximate indicator of water content, since olivine CPOs are thought to change their patterns with the amount of water in olivine crystals: producing A, B, C, D and E type fabrics (Karato et al., 2008). A or D fabrics would develop under anhydrous conditions, whereas B, C, or E fabrics would develop under water present conditions (Jung and Karato, 2001; Katayama et al., 2004). It is noted that AG type fabrics are also known to occur in nature (e.g., Michibayashi et al., 2016). Thus, olivine CPOs in peridotites are useful to detect water infiltration from a transform fault. In this study, I consider water infiltration along the transform fault based on mineral assemblages and CPO patterns of peridotites.

2. GEOLOGICAL SETTING

The Marion Fracture Zone lies on the ultraslow spreading SWIR at 33°30’E (Fig. 1) between the northern branch of the Andrew Bain FZ to the west and the Marion FZ to the east linked by two intervening 132 and 75 km long orthogonal magmatic segments. It offsets the SWIR 120 km to the northeast and is flanked by high transverse ridges that rise ~4 km above the floor of its ~35 km wide 5,200-m deep transform valley. The SWIR extends ~6,500 km northeast from the Bouvet to the Indian Ocean Triple Junction (Fig. 1).

Unlike fast spreading ridges, there is little evidence for steady-state magma chambers, as found at the East Pacific Rise due to the very low rate of magma supply, and overall the crust is thin and discontinuous (Zhou and Dick, 2013), often with widely spaced large volcanic segments that connect numerous transform faults and oblique amagmatic segments (e.g., Sauter 2010). This can produce very large variations in crustal thickness over relatively short (~100 km) length scales (e.g., Rommevaux, 1994; Schlindwein and Schmid, 2016; Zhao et al., 2013). Due to its rough topography, and variable magma budget, diabase, gabbro, peridotite and metamorphic rocks have been obtained by many dredge surveys (Fig. 1; e.g., Dick, 1989; Meyer et al., 1989; Dick et al., 2003; Seyler et al., 2003; Zhou and Dick, 2013; Sauter et al., 2013), making an ideal location for studying the lower crust and mantle, and the magmatic and tectonic processes underlying plate tectonics.

Mantle peridotites, mostly granular and porphyroclastic harzburgites were dredged from the Marion and adjacent Marion Transforms, associated with pillow basalt, diabase, and gabbro showing that the transform walls expose the lower crust and mantle (Fig. 1; Fisher et al., 1986). The mylonite peridotites, which are the focus of this study, were collected from the eastern wall of the Marion Transform (Dredges 18 and 19 in Fig. 1). Jaroslow et al. (1996) first reported these intensely deformed peridotite mylonites containing amphibole and chlorite. These authors report geothermometrically derived olivine-spinel equilibration temperatures of 633° to 844°C for four Dredge 18 peridotites (samples 2, 6, 23, and 40), representing the minimum temperatures for their crystal plastic deformation.

In this study, I used 7 peridotites derived by the dredge survey during PROTEA cruise in 1983 as samples for analyses (Table 1). Mylonitized peridotites such as my samples represent about 5% of all dredged abyssal peridotites. They have previously been collected in-situ from detachment fault footwalls at the Kane Megamullion (Dick et al., 2008) and the Atlantis Bank Oceanic Core Complex (Dick et al., 2019). As such they do not generally represent samples from the actual transform slip zone, however, they do represent high temperature mylonites that formed where the detachment fault rooted deep within the upper mantle at the ridge axis. Dick et al. (2008, 2019), however, suggest that the detachment fault turns into and merges with the transform-slip zone at ridge-transform intersections, forming a single fault system.

The Dredge 18 and 19 samples come from 5,100-4,800 and 3,900-2,700 m respectively on the Marion Transform wall (Fig. 1), and thus whereas the Dredge 19 samples likely represent detachment footwall mylonites, the Dredge 18 mylonites may have been uplifted by later transform parallel high-angle normal faulting from beneath the transform valley floor. In either case, however, it can be argued that these mylonites formed from similar parent mantle peridotite under conditions very similar to that in the transform slip zone.

3. METHODS

3. 1. Sample preparation for microstructural observation

30-μm thick thin sections were prepared on the plane perpendicular to the foliation and parallel to the lineation (XZ planes) defined by elongated and/or linearly arranged spinel and pyroxene grains. They were then polished using 1-μm diamond paste and colloidal silica for >5 hours for microstructural observations and analyses.

3.2. Major element compositions

Major element compositions of 7 samples were analyzed by electron microprobe (JEOL JXA-8900R). Thin sections were carbon coated by the thickness of ca. 360 nm to avoid charging during analyses. An accelerating voltage of 20 kV, probe current of 12 nA and beam diameter of 2 μm, with a count time of 10 s for 12 elements and 5 s for background were used. Ferric ion contents of spinel were determined by spinel stoichiometry.

3.3. Crystallographic-preferred orientations (CPOs)

CPO patterns of olivine grains in highly polished XZ thin sections were measured by using a scanning electron microscope (SEM) equipped with an electron back-scatter diffraction (EBSD) system (HITACHI S-3400N Type II with HKL Channel5). 20 kV accelerating voltage, and low vacuum mode (30 Pa) were used. I measured more than 200 crystal orientations per sample, and each crystal orientation was projected on lower hemisphere equal area stereo nets.

In this study, I used *J*-index as an measure of crystal orientation intensity, which takes the value of 1 when crystal orientations are completely random and infinite when those are single. The value of *J*-index is defined by

$$J = \int \mathrm{f}(\mathbf{g})^2 \mathrm{d}\mathbf{g}$$

where f(**g**) is texture function (Mainprice and Silver, 1993). $\mathbf{g} = (\varphi_1, \phi, \varphi_2)$ and $\mathrm{d}\mathbf{g} = 1/8\pi^2 \mathrm{d}\varphi_1 \mathrm{d}\phi \mathrm{d}\varphi_2$ with triplet of Euler angles φ_1, ϕ, φ_2, respectively.

CPO patterns of peridotites can be evaluated quantitatively in comparison with P-wave seismic velocities (Michibayashi, 2015; Michibayashi et al., 2016). To define the field of the six olivine fabric types (i.e. A, B, C, D, E and AG types) in a diagram, I should consider the orientations of the three principal axes in the structural framework (X, Y, Z-axes) where the foliation is the XY plane and the lineation is parallel to the X-axis. Thus, V_x is the velocity parallel to the X-axis, V_y is parallel to the Y-axis, and V_z is parallel to the Z-axis. I used a Flinn diagram (Flinn, 1969) to characterize the CPO patterns and evaluate the fabric intensities based on hand specimens P-wave anisotropies. In this diagram, Vx/Vy and Vy/Vz as the ratios of the P-wave velocities in directions of X, Y, Z-axis of the samples are vertical axis and horizontal axis, respectively, and (1, 1) is origin (Michibayashi et al., 2016). In this way, the fabric-index-angles for the six olivine fabric types have been defined by the angle of inclination between the origin and a point in the diagram: 63° for A type, -28° for B type, 158° for C type, 90° for D type, 106° for E type and 0° for AG type (Michibayashi et al., 2016).

EBSD analysis provides not only crystal orientations but also phase information. Phase maps were obtained by using step sizes of 2.5 to 5 μm. I used HKL Channel5 software to process map data by removing single pixels that differed >10° and extrapolating non-indexed pixels with average orientation of neighboring 4 pixels.

4. RESULTS

4.1. Microstructures

Five samples (D19-86, D19-5, D19-2, D19-85 and D18-12; Fig. 2a-e) have heterogeneous textures consisting of variously deformed coarse grains and anastomosing fine-grained domains, whereas two samples (D19-58 and D19-47; Fig. 2f-g) are ultramylonites consisting of an extremely fine-grained matrix with several porphyroclast grains. The two ultramylonites exhibit alternately arranged multi-layer structures of olivine and amphibole, where the layers have variable thickness. One of the ultramylonites (D19-47; Fig. 2g) also has microfolds and shear bands.

Figure 3 shows the phase maps, where white and black lines are subgrain boundaries (misorientation angles are 2° to 10°) and grain boundaries (>10°), respectively. Peridotites with heterogeneous textures include olivine, orthopyroxene, clinopyroxene and spinel as coarse-grained crystals and amphibole as fine-grained matrix, and its grain sizes range from a few micrometers to several millimeters (Fig. 3a-e). D19-86 (Fig. 3a), D19-5 (Fig. 3b) and D19-2 (Fig. 3c) contain amphiboles with few subgrain boundaries that cut olivine and pyroxene crystals, whereas D19-85 (Fig. 3d) and D18-12 (Fig. 3e) contain fine-grained amphiboles with subgrain boundaries. Ultramylonites contain olivine, spinel and amphibole occurring as both matrix and porphyroclasts, whose sizes are less than 20 μm, and ~1.5 mm respectively (Fig. 3f-g). D18-12 (Fig. 3e) and two ultramylonites (Fig. 3f-g) include large amounts of amphibole and minor pyroxene.

4.2. Major element compositions

Major element compositions of olivine, spinel and amphiboles are shown in Fig. 4 and Tables 2-4. Olivine grains in 7 peridotites have generally homogeneous compositions. The Mg# [=Mg/(Mg+Fe)] of olivine are almost constant, ranging from 0.895 to 0.912 (Table 2). Spinel grains have Mg# values of 0.594 to 0.740 and Cr# [=Cr/(Cr+Al) atomic ratio] of 0.171 to 0.339. TiO_2 contents of all spinel grains are less than 0.15 wt.% (Table 2) indicating that these were nearly pure residues of mantle melting with little or no late-stage melt impregnation (e.g., Dick and Bullen, 1984). These values are similar to those of other abyssal peridotites (Fig. 4b, c), and chemical components of both olivine and spinel grains plot inside of OSMA (Arai, 1994), indicating that they were derived from mantle peridotites, regardless of their textures and occurrence of amphibole (Fig. 4a). Amphiboles have high Mg# values (> 0.9), and range in composition from tremolite to magnesio-hornblende and pargasite (Fig. 4d-e).

4.3. Crystallographic-preferred orientations (CPOs)

The transform peridotite CPO patterns are shown in the XZ reference frame in Fig. 5. Those samples with deformed amphiboles and subgrain boundaries and those with undeformed amphiboles with few subgrain boundaries are significantly different. Those containing undeformed amphiboles with few subgrain boundaries, D19-2, D19-5 and D19-86, show A to D type fabric (Fig. 5a-c). The two mylonites, D19-47 and D19-58, as well as D18-12 and D19-85, all of which have deformed amphiboles and sub-grain boundaries show B and E type or random fabrics (Fig. 5d-g). Ultramylonite D19-58 with deformed amphiboles shows a complicated fabric (Fig. 5f) exhibiting a tendency to c-axis slip. *J*-indices range from 1.63 (D18-12; Fig. 5e) to 4.58 (D19-47; Fig. 5g).

Figure 6 shows the Flinn diagram plot for the P-wave velocity (*Vp*) anisotropies (right panel in Fig. 5) calculated for my samples based on the olivine CPO data, elastic coefficients, and density of a single olivine crystal (Mainprice, 1990), where each zone of the six fabric types is defined following to Michibayashi et al. (2016). The ratio of *Vy/Vz* and *Vx/Vy* of ultramylonite D19-47 plots in the B type zone, whereas that of the other ultramylonite D19-58 plots near the A type zone. The ratios of D18-12 and D19-85 showing heterogeneous textures are in the B and E type zones, respectively. Those of D19-2 and D19-5 are plotted in the A type zone, and D19-86 is in the D type zone.

D19-47 shows the strongest *Vp* anisotropy (A*Vp* = 8.19%), whereas D18-12 shows weakest anisotropy (A*Vp* = 2.10%), the others indicate moderate strength (A*Vp* = 5.06-7.37%). There is a positive correlation between *J*-indices and the values of A*Vp*.

5. DISCUSSION

5.1. Deformation of peridotites

There are several studies reporting deformed peridotites obtained from transform fault. Jaroslow et al. (1996) reported mylonitic peridotites derived from the transform faults along the SWIR. They concluded that the textures were formed by strain localization accompanied by decrease in temperature. Moreover, they referred to hydrothermal alteration of peridotites due to the existence of hydrous minerals.

Peridotites analyzed in this study show ultramylonitic or heterogeneous textures with coarse-grained olivine and pyroxene crystals and fine-grained domains. It shows that strain partitioning and grain size reduction occurred in these peridotites. Additionally, these peridotites have fine-grained amphiboles in their matrix. Karato and Jung (2003) reported that water significantly decreases viscosity of peridotite. The presence of water may have influenced not only the formation of amphiboles but also strain partitioning during deformation.

5.2. P-T conditions and generation of hydrous minerals

Amphibole peridotites and amphibole-chlorite peridotite are stable under ~1400 MPa (Jenkins, 1981). Spinel ($MgAl_2O_4$) is stable above ~800 MPa, and at lower pressure, it reacts with orthopyroxene and clinopyroxene to produce plagioclase (Jenkins, 1981). There are spinel peridotites and spinel/plagioclase peridotites both containing amphibole and locally chlorite (Fig. 3). Hence, it suggests that water infiltrated the peridotites under the pressure conditions of 1,400 MPa or less (Fig. 7).

These peridotites contain several hydrous minerals, which occur under different temperature conditions. The constituent minerals of peridotite react with water at different temperatures. Pyroxenes react preferentially with water to produce amphibole under high temperature condition (~800 °C):

$$\mathrm{Opx} + \mathrm{Cpx} + \mathrm{Sp} + H_2O \rightarrow \mathrm{Amp} + \mathrm{Fo}$$

where Opx, Cpx, Sp, Amp and Fo in the above formula are orthopyroxene, clinopyroxene, spinel, amphibole and forsterite, respectively. At lower temperature (~600 °C), Chlorite is generated by the following equations:

$$\mathrm{Opx + Sp + Fo + H_2O \rightarrow Chl}$$

$$\mathrm{Amp + Fo \rightarrow Opx + Cpx + Chl + H_2O}$$

where Chl is chlorite. As the temperature further drops, serpentines appear by reactions of olivine, pyroxene, amphibole (tremolite) and water (< 400 °C).

All samples include amphibole, and D19-5 has also chlorite (Fig. 3). Additionally, although samples show serpentine veins, no samples have anthophyllite and talc. These features indicate that they were affected by water until the temperatures drop down from ~800 °C to lower than 400 °C. The lack of anthophyllite and talc implies that hydration of peridotite proceeds at higher temperature than 700 °C (Fig. 7). The existence of peridotites containing large amounts of amphibole and small amounts of pyroxenes (Fig. 3) suggests that consumption of pyroxenes advanced by hydration under that temperature condition.

5.3. CPOs of peridotites derived from the transform fault

Peridotite develops different olivine CPO patterns depending on water content during deformation (Karato et al., 2008). Water-poor (< 200 H/10^6Si) peridotite develops A or D type fabric, while peridotite with moderate to saturated amount of water (200~1310 H/10^6Si) develops a B, C or E type fabric depending on differential stress. Therefore, the CPO pattern can be used as an approximate indicator of peridotite water content during deformation. There are many studies suggesting the presence of water during peridotite deformation based on the olivine fabrics (e.g., Mizukami et al., 2004; Tasaka et al., 2008; Skemer et al., 2010; Muramoto et al., 2011; Michibayashi and Oohara, 2013; Johanesen and Platt, 2015; Czertowicz et al., 2016; Hidas et al., 2016; Précigout et al., 2017; Kohli and Warren, 2020; Prigent et al., 2020).

In previous studies, pole figures projected on equal area, lower hemisphere nets have been used to exhibit olivine fabrics. Recently, *Vp*-Flinn diagrams with Vx/Vy on the vertical axis, and Vy/Vz on the horizontal axis with (1, 1) for the point of origin have been used (Fig. 6; e.g., Michibayashi, 2015; Michibayashi et al., 2016; Soustelle and Manthilake, 2017). This allows evaluation of CPO patterns quantitatively by the angle of inclination between the origin and a point in the diagram (θ) and distance from the origin (Fig. 6). In this study, the three samples (D19-5, D19-5 and D19-86) with undeformed amphiboles with only a few subgrain boundaries show A to D type fabrics (Figs. 5 and 6), while two samples (D19-85 and D19-47) containing deformed amphiboles with subgrain boundaries show B and E type fabrics in the pole figures (Figs. 5 and 6). Thus, amphibole formed after deformation in the samples with A to D type fabrics, while amphibole formed before or during deformation in those with B and E type fabrics.

One heterogeneous structured peridotite (D18-12) with deformed amphiboles shows a random fabric in the pole figure (Fig. 5e), but the calculated seismic plots on the line of B type fabric near the origin in a *Vp*-Flinn diagram (Fig. 6). This indicates the specimen developed a weak B type fabric during deformation with amphibole. Ultramylonite D19-58 has a complicated fabric (Fig. 5f) that shows a tendency to c-axis slip and plots in the A type field of the Flinn diagram (Fig. 6). Based on the presence of deformed amphibole in this sample, the fabric in Fig. 5f would have formed by slip on both (001)[100], resulting in an E type fabric, and the (010)[001] slip system resulting in B type fabric, which implies the presence of water during deformation. As a consequence, these observations are consistent with Karato et al.'s (2008) results as amphibole formation requires water, suggesting that the peridotites deformed under hydrous condition.

5.4. Hydrous shearing under the transform fault

It has been previously pointed out that water enters into the Earth's interior from transform fault (e.g., Francis, 1981; Tucholke and Lin, 1994; Kerric, 2002; Roland et al., 2010). These studies imply that water infiltrates lithospheric mantle at a transform fault because of the existence of serpentines and thermal structure of transform fault. In this study, the peridotite ultramylonites have amphibole porphyroclasts (Fig. 3f), which indicates that they formed prior to deformation, while the heterogeneous textured peridotites contain amphibole in the matrix (Fig. 3a, c-d), which indicates that amphibole crystallized before and/or during deformation. Furthermore, the existence of peridotites containing undeformed amphibole (Fig. 3b) indicates that amphibole was generated continuously before, during, and after deformation. These observations suggest that water infiltrated the transform fault during shearing (Fig. 8).

Also, minerals such as amphibole, chlorite, spinel and plagioclase in peridotite (Fig. 3) can indicate an approximate pressure during their formation, and consequently depth water infiltrated the shear zone. The presence of chromian spinel $(Mg,Fe)(Cr,Al,Fe)_2O_4$ suggests pressures condition of less than the transition from pure spinel ($MgAl_2O_4$) to plagioclase peridotite, corresponding to depth less than ~40 km (i.e., 1400 MPa; Fig. 7; Jenkins, 1981). The textures, mineral assemblages and olivine fabrics all indicate water infiltration during formation of these mylonites. In contrast, typical abyssal peridotites do not contain primary or secondary high temperature amphiboles, including those dredged in the adjacent transforms.

Active deformation raises permeability in rocks, this creates a negative pressure gradient that draws in fluid and volatiles into shear zones and fault systems. As a result, fault systems studied on land are frequently the location of hydrothermal ore deposits due to the localization of fluid flow along them. Based on my results and previous work, I propose that deformation of the peridotite takes place under hydrous condition, with water infiltration and shearing occur at the same time under the transform fault (Fig. 8).

The source of the water would be important to identify. It could be seawater percolating down into the fault system at depth (Fig. 8), or it could be derived from the host peridotite or fluids from gabbroic intrusions at depth. Given the presence of high-temperature amphiboles, this could have occurred at temperatures up to ~800°C, perhaps higher. Kurz et al. (2009) have found that mantle-derived helium is concentrated in high temperature mylonite peridotites from the SW Indian Ridge and from the Josephine Ophiolite in Oregon – which leaves open the real possibility that the water is also juvenile, rather than seawater derived.

My sample locations range from high to low on the eastern Marion Transform wall (Fig. 1). Only 5% of the peridotites dredged from transform walls are mylonites (Dick, 1989). Moreover, mylonites do not occur randomly in peridotite dredge hauls. Rather virtually the entire haul is mylonite, or they are all protogranular and porphyroclastic peridotites (Dick, 1989). In general, the dredge samples represent loose talus, and rarely is there evidence that they are ripped from outcrop. Most represent debris fields produced by landslips. This is consistent with peridotite mylonites sampled in-situ on detachment footwalls, representing thick zones of shear deformation likely less than a few hundred meters underlain by massive granular peridotite.

The mylonites dredged from the base of the transform wall might be uplifted by late faulting from the transform slip zone, but it is more likely that they also represent the detachment fault shear zone as it turns into and merges into the transform slip zone below the transform wall (Dick et al., 2019). This becomes the western branch of a fault flower structure formed by the extension of the opposing detachment fault intersections with the transform slip zones as at the Kane Megamullion on the MAR and at Atlantis Bank on the SWIR (see Dick et al., 2008, 2019).

Based on seismic studies, however, the primary slip zone in the transform is the central vertical branch of the flower structure, not the branches that extend upward to the transform walls, and merged with the detachment faults at the ridge transform intersections. The conditions of formation of these mylonites, however, should replicate those in the principle transform slip zone and show that water-influenced high-temperature granulite facies deformation must be occurring at depth within the main transform slip zone with a consequent negative effect on its strength and viscosity.

6. CONCLUSIONS

In this study, I analyzed 7 deformed peridotites derived from Marion transform fault, the SWIR. These samples include ultramylonites and heterogeneous textured peridotites. Ultramylonites show layering structures with extremely fine-grained matrix and porphyroclasts composed of olivine, amphibole and spinel. Heterogeneous-textured peridotites show fine-grained matrix and coarse-grained crystals of olivine, pyroxenes and spinel. Ultramylonites and two out of heterogeneous-textured specimens exhibit deformed structures of amphiboles.

The major element compositions of olivine and spinel indicate that these were likely typical residues of mantle melting prior to deformation. Amphiboles have chemical components of tremolite, magnesio-hornblende and pargasite, indicating a range of conditions for infiltration of water, which may have either a seawater or juvenile origin – or both.

Three samples have not only spinel but also plagioclase. This implies that hydration of these peridotites occurred at low pressure. The presence of amphibole, chlorite and serpentine means these peridotites were affected by water from ~800 °C to <500 °C.

Olivine CPO patterns are significantly different between specimens including non-deformed amphiboles and those including deformed amphiboles. Specimens with non-deformed amphiboles show A to D type fabric, which are assumed to represent deformation under water-poor conditions. On the other hand, specimens including deformed amphiboles show B and E type fabric, but one ultramylonite, which indicated deformation in the presence of moderate to large amounts of water. The one ultramylonite exhibits complicated fabric showing a tendency of c-axis slip, which also implies the effect of water. Given that the conditions of formation of these mylonites should be the same as those in the central slip zone of the transform, this indicates that there should be a significant effect of water on the strength of the lithosphere in the transform domain below the zone of serpentinization.

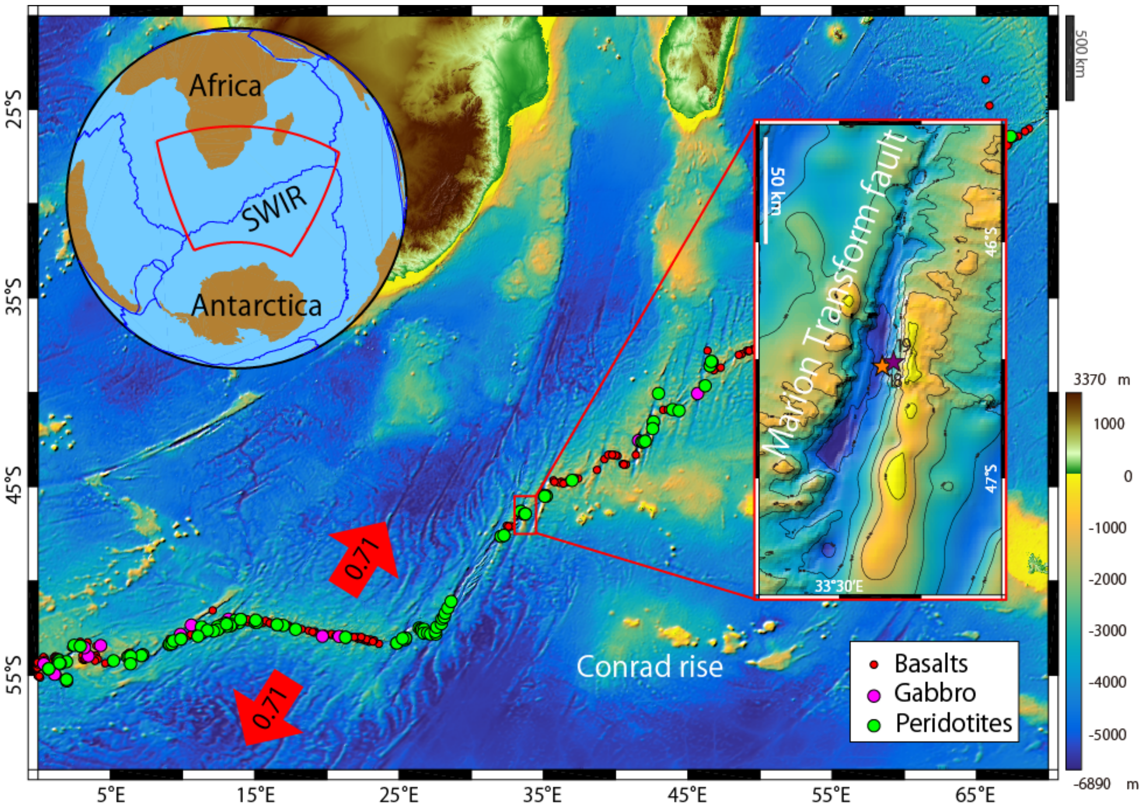

Figure 1. Location of the Southwest Indian Ridge (SWIR) and the Marion transform fault. Numbers on red arrows indicates spreading rate. Dredges 18 and 19 on enlarged map of the Marion transform fault indicate the sampling sites of analyzed samples in this study (18 for PROTEA.5 D18 and 19 for PROTEA.5 D19).

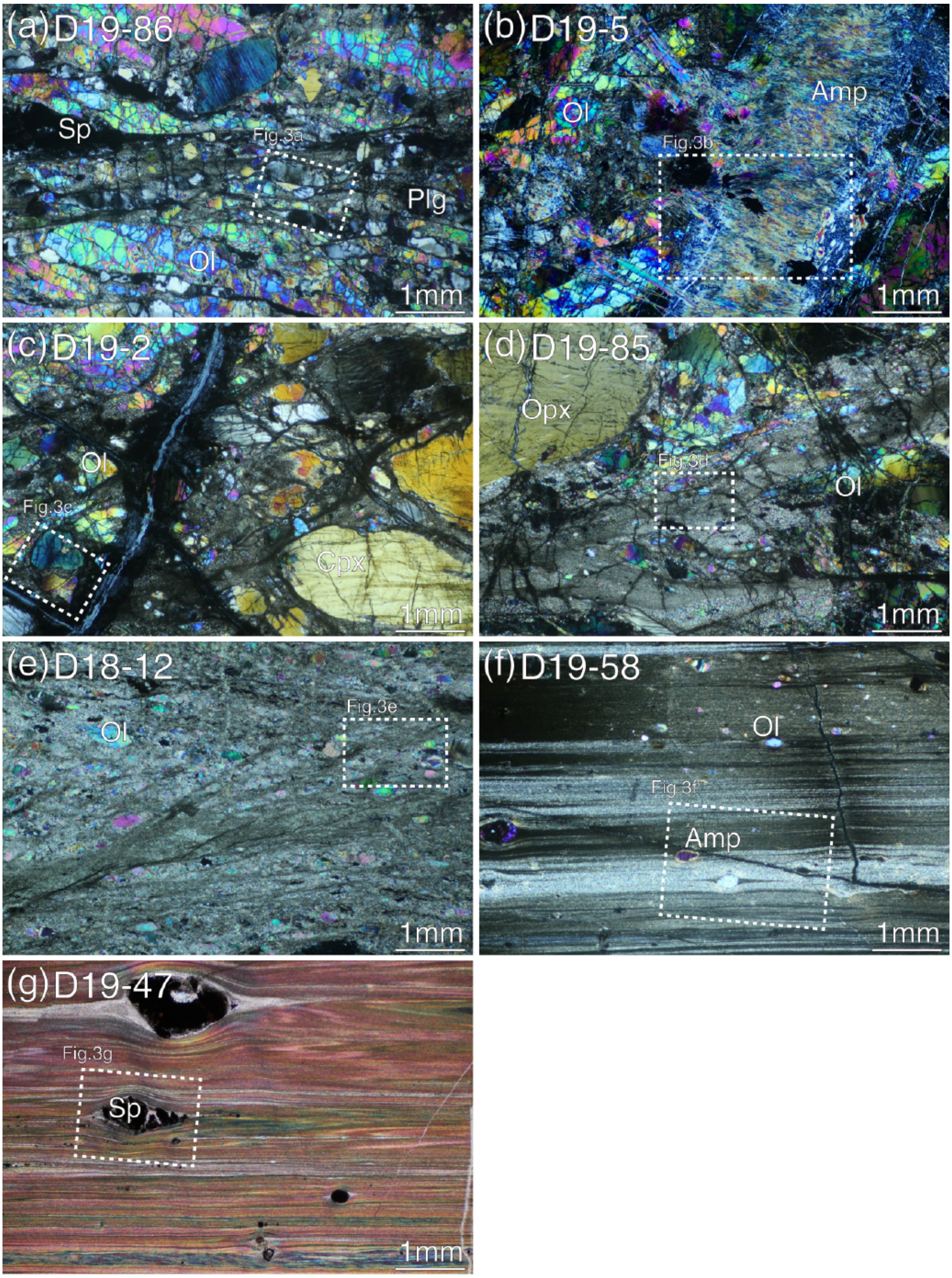

Figure 2. Photomicrographs of the peridotites derived from the Marion transform fault. (a)-(e) Heterogeneous-textured peridotites. (f) and (g) Ultramylonites. Abbreviation: Ol = olivine, Cpx = clinopyroxene, Opx = orthopyroxene, Sp = spinel, Plg = plagioclase, Amp = amphibole

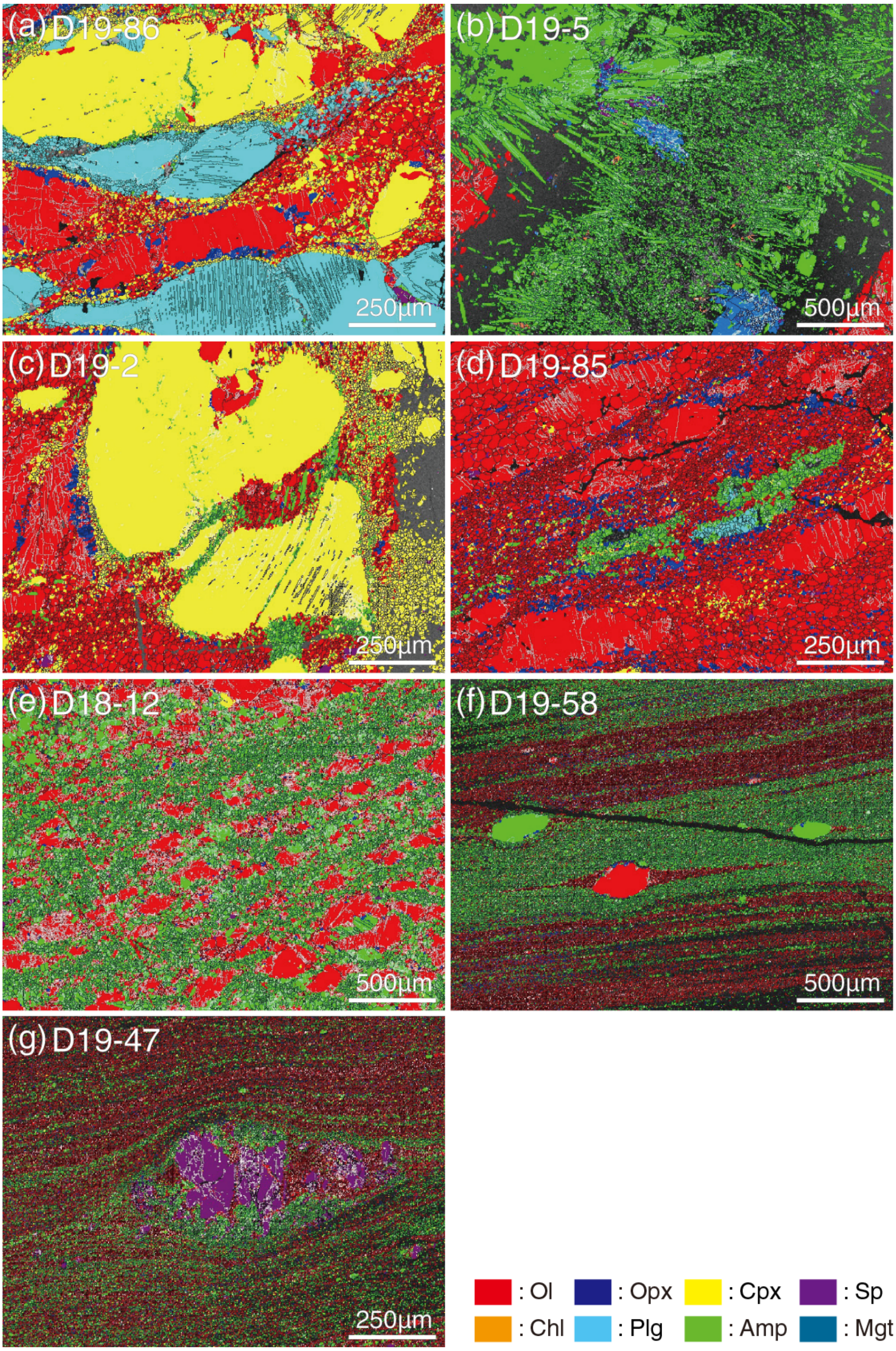

Figure 3. Phase maps of peridotites shown the area indicated by white dotted squares in Fig.2. Abbreviation: Ol = olivine, Cpx = clinopyroxene, Opx = orthopyroxene, Sp = spinel, Plg = plagioclase, Amp = amphibole, Chl = chlorite, Mgt = magnetite

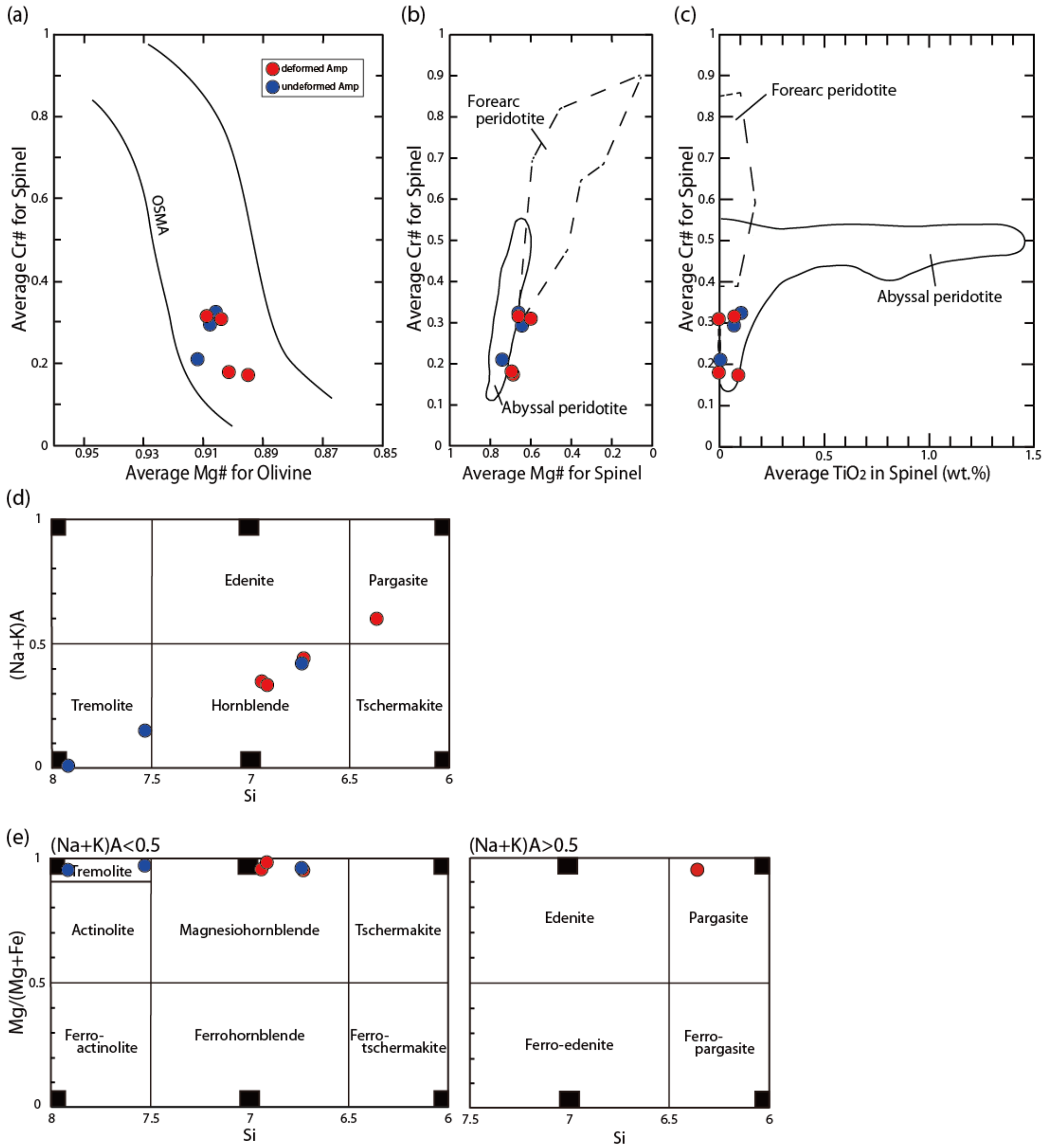

Figure 4. Chemical characteristics of peridotites. (a) Relationship between Mg# (= Mg/(Mg + Fe)) for olivine and Cr# (= Cr/(Cr + Al)). (b) Relationship between Mg# and Cr# for spinel. (c) Relationship between TiO2 wt.% and Cr# for spinel. (d) and (e) Chemical characteristics of amphibole crystals.

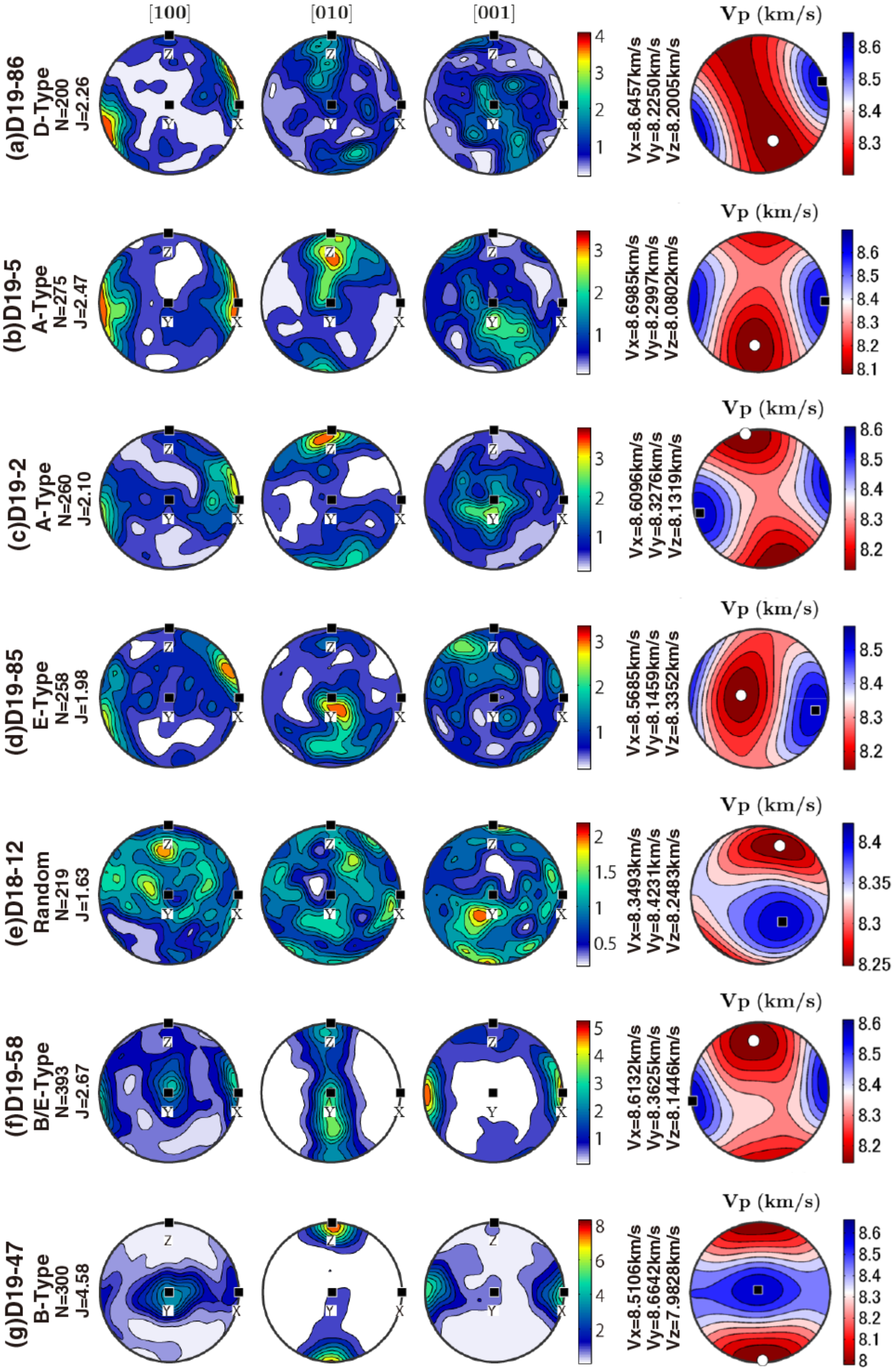

Figure 5. CPO patterns of olivine projected on equal area, lower hemisphere with XZ reference flame. Foliation is horizontal (XY plane) and lineation is E-W (X axis). Contours are multiples of uniform distribution. J is J-index indicating fabric strength and N is number of measurement point. P-wave velocities are shown on the right side with filled black squares and white circles as direction of maximum and minimum P-wave velocities, respectively.

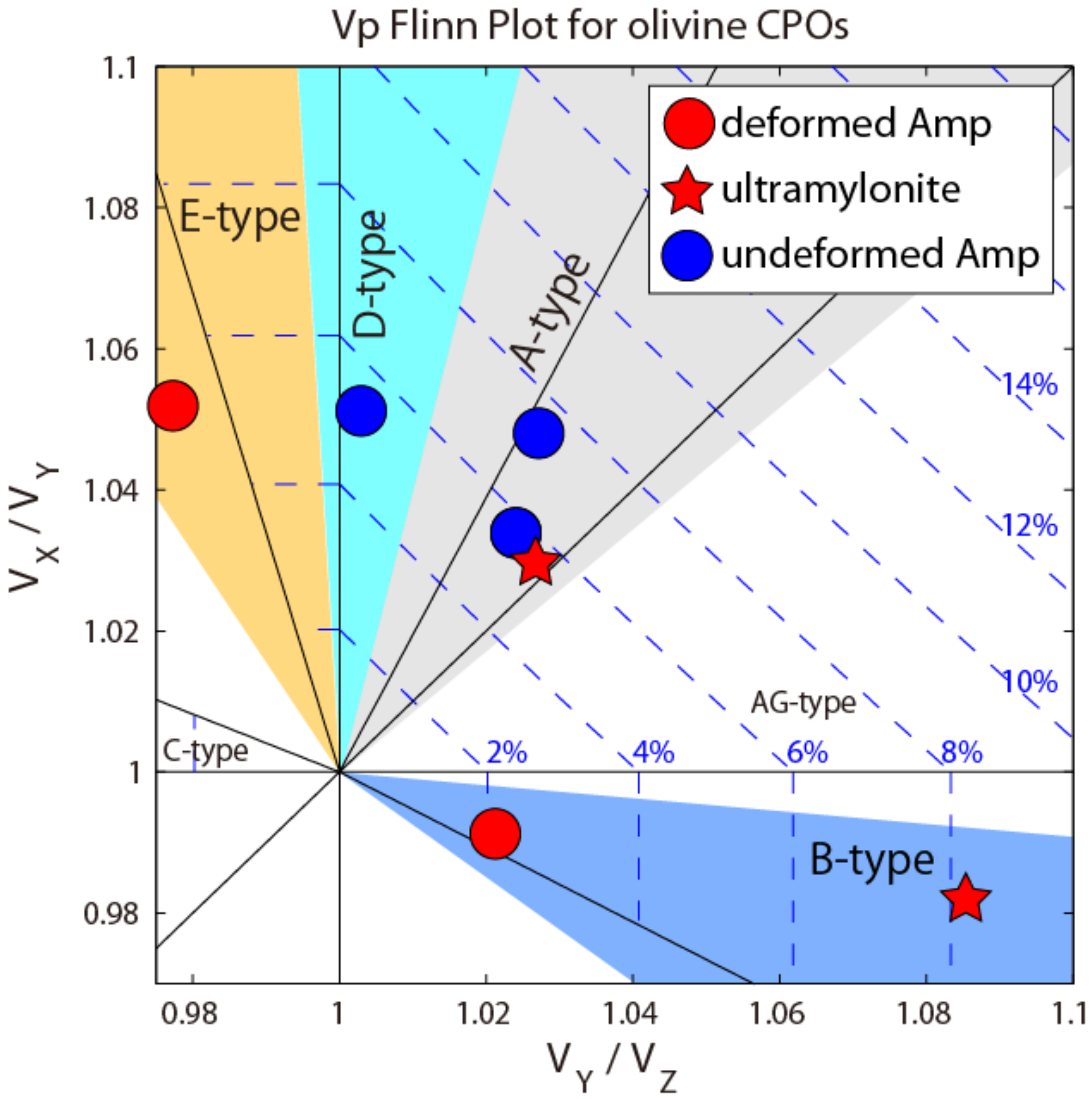

Figure 6. Flinn diagram with Vx/Vy for vertical axis, Vy/Vz for horizontal axis and (1,1) for the origin. Fabric types of olivine and intensities of Vp anisotropies depend on the angle of inclination between the origin and the point in the diagram and distances from the origin, respectively. Circles for heterogeneous-textured peridotites with various grain sizes, stars for ultramylonites. Red legends (circle and star) exhibit peridotites with deformed amphibole, whereas blue circle exhibits peridotites with undeformed amphibole.

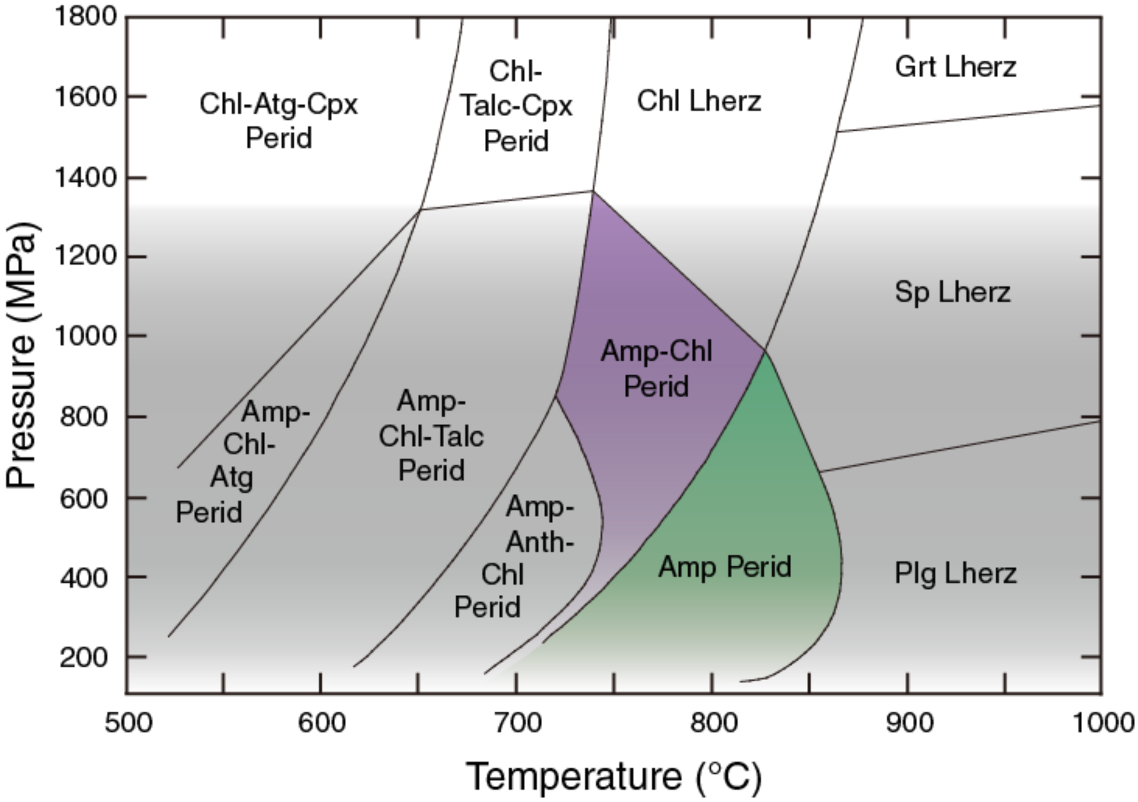

Figure 7. Phase diagram of peridotite containing water modified after Jenkins (1981). Green and purple-shaded areas show possible P-T conditions of peridotites analyzed in this study. Abbreviation: Perid = peridotite, Lherz = lherzolite, Grt = garnet, Sp = spinel, Plg = plagioclase, Amp = amphibole, Chl = chlorite, Anth = anthophyllite, Talc = talc, Atg = antigorite

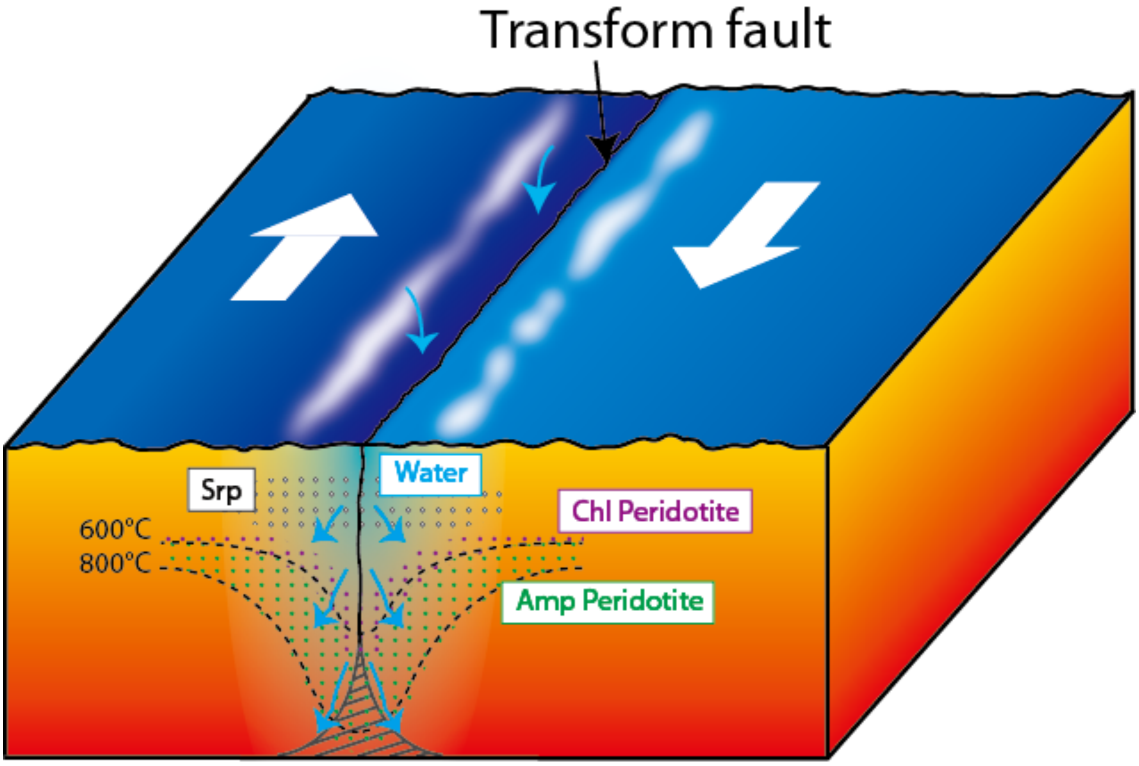

Figure 8. Schematic diagram illustrating water infiltration from a transform fault and possible hydrous minerals contained in peridotite. Dotted lines are isotherms of 600 °C and 800 °C. Area shaded by gray lines is ductile shear zone. Abbreviation: Amp = amphibole, Chl = chlorite, Srp = serpentine

Table 1. Sampling sites of the peridotites.

Dr	Sample Number	Lat	Lon	Depth (m)	Texture	Location
18	12	-46.525	33.763	5100	Heterogeneous texture	East Wall of Marion Transform fault
19	2	-46.507	33.832	3900	Heterogeneous texture	East Wall of Marion Transform fault
19	5	-46.507	33.832	3900	Heterogeneous texture	East Wall of Marion Transform fault
19	47	-46.507	33.832	3900	Ultramylonite	East Wall of Marion Transform fault
19	58	-46.507	33.832	3900	Ultramylonite	East Wall of Marion Transform fault
19	85	-46.507	33.832	3900	Heterogeneous texture	East Wall of Marion Transform fault
19	86	-46.507	33.832	3900	Heterogeneous texture	East Wall of Marion Transform fault

Table 2. Major element compositions of olivine. The values are averages for each sample.

Sample	(a) D19-86	(b)D19-5	(c) D19-2	(d) D19-85	(e) D18-12	(f) D19-58	(g) D19-47
No. of analysis	10	28	21	14	16	22	4
SiO_2	40.33	40.65	40.62	40.32	40.57	41.64	40.39
TiO_2	0.01	0.01	0.01	0.00	0.01	0.01	0.00
Al_2O_3	0.01	0.10	0.03	0.02	0.04	0.25	0.08
FeO	9.08	9.25	8.67	8.90	10.20	9.18	9.59
MnO	0.13	0.14	0.12	0.13	0.14	0.04	0.13
MgO	50.19	50.02	50.50	49.87	48.92	48.76	49.26
CaO	0.01	0.02	0.00	0.01	0.04	0.04	0.06
Na_2O	0.00	0.01	0.00	0.01	0.02	0.01	0.02
K_2O	0.00	0.00	0.00	0.00	0.01	0.00	0.00
Cr_2O_3	0.00	0.05	0.03	0.03	0.03	0.05	0.01
NiO	0.22	0.23	0.26	0.22	0.22	0.01	0.22
Total	99.98	100.46	100.24	99.51	100.18	99.99	99.78
Cations							
Si	0.99	0.99	0.99	0.99	1.00	1.01	0.99
Ti	0.00	0.00	0.00	0.00	0.00	0.00	0.00
Al	0.00	0.00	0.00	0.00	0.00	0.01	0.00
Fe	0.19	0.19	0.18	0.18	0.21	0.19	0.20
Mn	0.00	0.00	0.00	0.00	0.00	0.00	0.00
Mg	1.83	1.82	1.83	1.83	1.79	1.77	1.80
Ca	0.00	0.00	0.00	0.00	0.00	0.00	0.00
Na	0.00	0.00	0.00	0.00	0.00	0.00	0.00
K	0.00	0.00	0.00	0.00	0.00	0.00	0.00
Cr	0.00	0.00	0.00	0.00	0.00	0.00	0.00
Ni	0.00	0.00	0.01	0.00	0.00	0.00	0.00
Total	3.01	3.01	3.01	3.01	3.00	2.98	3.01
Mg#	0.91	0.91	0.91	0.91	0.90	0.90	0.90

Table 3. Major element compositions of spinel. The values are averages for each sample.

Sample	(a) D19-86	(b) D19-5	(c) D19-2	(d) D19-85	(e) D18-12	(f) D19-58	(g)D19-47
No. of analysis	4	11	5	16	10	18	22
SiO_2	0.13	0.07	0.08	0.07	0.11	0.11	0.07
TiO_2	0.07	0.11	0.01	0.07	0.09	0.00	0.03
Al_2O_3	39.14	40.53	49.16	40.58	51.11	37.89	50.63
Fe_2O_3	1.55	1.68	1.41	2.17	1.53	4.91	1.89
FeO	14.94	14.51	11.50	14.51	13.86	16.39	13.51
MnO	0.21	0.20	0.15	0.19	0.14	0.06	0.14
MgO	15.21	15.85	18.37	15.66	16.84	13.64	17.11
CaO	0.07	0.01	0.00	0.01	0.05	0.00	0.02
Na_2O	0.01	0.01	0.00	0.02	0.03	0.04	0.01
K_2O	0.00	0.00	0.00	0.00	0.00	0.00	0.00
Cr_2O_3	29.56	28.77	19.43	27.61	15.73	25.13	16.34
NiO	0.07	0.10	0.13	0.09	0.14	0.05	0.15
Total	100.98	101.83	100.25	100.98	99.65	98.23	99.91
Cations							
Si	0.00	0.00	0.00	0.00	0.00	0.00	0.00
Ti	0.00	0.00	0.00	0.00	0.00	0.00	0.00
Al	1.29	1.32	1.55	1.34	1.62	1.31	1.61
Fe^{3+}	0.03	0.04	0.03	0.05	0.03	0.11	0.04
Fe^{2+}	0.35	0.34	0.26	0.34	0.31	0.40	0.30
Mn	0.01	0.00	0.00	0.00	0.00	0.00	0.00
Mg	0.64	0.65	0.74	0.65	0.68	0.59	0.69
Ca	0.00	0.00	0.00	0.00	0.00	0.00	0.00
Na	0.00	0.00	0.00	0.00	0.00	0.00	0.00
K	0.00	0.00	0.00	0.00	0.00	0.00	0.00
Cr	0.66	0.63	0.41	0.61	0.34	0.58	0.35
Ni	0.00	0.00	0.00	0.00	0.00	0.00	0.00
Total	2.99	2.99	3.00	3.00	3.00	3.00	3.00
Mg#	0.64	0.66	0.74	0.66	0.68	0.60	0.69
Cr#	0.34	0.32	0.21	0.31	0.17	0.31	0.18

Table 4. Major element compositions of amphibole. The values are averages for each sample.

Sample	(a) D19-86	(b) D19-5	(c) D19-2	(d) D19-85	(e) D18-12	(f) D19-58	(g) D19-47
No. of analysis	5	3	3	2	4	7	12
SiO_2	48.17	56.81	54.49	44.74	49.54	49.82	47.48
TiO_2	1.22	0.09	0.11	0.51	0.41	0.49	0.63
Al_2O_3	9.66	0.78	4.25	14.21	8.64	8.59	10.33
FeO	3.13	2.28	2.00	3.40	3.24	3.75	3.63
MnO	0.06	0.08	0.04	0.05	0.07	0.02	0.06
MgO	20.02	22.69	22.13	18.12	19.92	21.66	19.14
CaO	12.27	12.76	12.77	12.25	12.05	10.85	12.40
Na_2O	1.71	0.18	0.73	2.32	1.50	1.32	1.76
K_2O	0.04	0.00	0.02	0.05	0.03	0.04	0.09
Cr_2O_3	0.84	0.16	0.31	0.29	0.52	0.07	0.53
NiO	0.00	0.01	0.01	0.01	0.07	0.53	0.01
Total	97.12	95.83	96.83	95.94	95.98	97.14	96.06
Cations							
Si	6.74	7.92	7.53	6.36	6.98	6.91	6.73
Ti	0.13	0.01	0.01	0.05	0.04	0.05	0.07
Aliv	1.26	0.08	0.47	1.64	1.02	1.09	1.27
Alvi	0.33	0.04	0.22	0.74	0.41	0.32	0.45
Fe^{3+}	0.21	0.03	0.09	0.21	0.19	0.35	0.24
Fe^{2+}	0.15	0.24	0.14	0.19	0.19	0.08	0.19
Mn	0.01	0.01	0.00	0.01	0.01	0.00	0.01
Mg	4.18	4.71	4.56	3.84	4.18	4.48	4.04
Ca	1.84	1.91	1.89	1.87	1.82	1.61	1.88
Na	0.46	0.05	0.20	0.64	0.41	0.36	0.48
K	0.01	0.00	0.00	0.01	0.00	0.01	0.02
Cr	0.09	0.02	0.03	0.03	0.06	0.01	0.06
Ni	0.00	0.00	0.00	0.00	0.01	0.06	0.00
Total	15.41	15.01	15.15	15.60	15.33	15.33	15.44
Mg#	0.96	0.95	0.97	0.95	0.96	0.98	0.95
(Na+K)A	0.42	0.01	0.15	0.60	0.34	0.33	0.44

Part2

Hydrous inclusions in olivine grains as an evidence of water infiltration along transform fault: Marion transform fault, Southwest Indian Ridge

ABSTRACT

Transform faults are shear zones along oceanic ridges and have been considered as entrances of water into upper mantle. Peridotites with hydrous minerals such as amphibole and chlorite suggest that water infiltration along transform faults, while inclusions consisting of fluids and/or hydrous minerals can also be an evidence of water infiltration. In this study, I described and measured 43 olivine-hosted inclusions in 11 peridotites derived from Marion transform fault, Southwest Indian Ridge by optical microscope and Raman spectroscopy. The inclusions consist of low-temperature serpentine, hydrogen and coexisting methane and graphite. Furthermore, the peridotites contain also amphiboles. Therefore, it is suggested that water infiltrated into shallow upper mantle where the temperature is up to ~800 °C and trapped in olivine grains, then after temperature dropped, reacted with host olivine to form low-temperature serpentine, hydrogen and coexisting methane and graphite. A series of reaction requires water, thus inclusions of hydrous minerals and/or hydrogen, methane and graphite indicate water infiltration along the transform fault.

1. INTRODUCTION

Transform faults are offsets along oceanic ridges, dividing ridge axes of ridges into segments. These offsets are strike-slip faults where oceanic plates formed on ridges pass each other, the direction of fault motion depends on the direction of plate motion due to seafloor spreading. In transform faults, seismic activities and deformed rocks due to fault motion has been observed. Roland et al. (2010) has constructed the model that explains thermal structure of transform fault and concluded that spatial distribution of earthquake along oceanic transform fault can be predicted more accurately with water infiltration based on several simulations. It has been pointed out that transform faults are shear zones on the seafloor that act as water inlets to the upper mantle (e.g., Francis, 1981; Kerric, 2002). Jaroslow et al. (1996) described hydrous minerals in ultramafic rocks derived from the fracture zones along Southwest Indian Ridge (SWIR) and Mid-Atlantic Ridge (MAR). They proposed that temperature of hydrothermal alteration of the peridotites was in the range of 350~700 °C based on the existence of amphibole, chlorite and serpentine.

In Part 1 study, deformation of hydrous minerals and CPOs of olivine formed under hydrous ccondition were described. In addition to these features, hydrous inclusion can be cited as an evidence of water infiltration. Klein et al. (2019) found fluid inclusions with methane (CH_4) and hydrogen (H_2) in gabbros and peridotites from wide range of tectonic settings by Raman spectroscopy. They discussed change in equilibrium compositions of olivine-hosted inclusions by thermodynamic modeling and concluded that the inclusions had been trapped in olivine above ~400 °C, and CH_4 and H_2 had occurred by serpentinization below ~340 °C. Kohli and Warren (2020) reported planar structures of fluid inclusions in mylonitic peridotites derived from Shaka fracture zone, SWIR. Their study proposed that formation process of the planar structures of fluid inclusions; cracks in olivine grains were formed by temporary change in differential stress due to earthquakes, then water infiltrated into the cracks, finally the cracks were healed and water was trapped in olivine grains as fluid inclusions. The purpose of Part 2 study is to consider water infiltration along the transform fault from a different aspect from Part1 study based on the existence of hydrous inclusions.

2. METHODS

2.1. Samples

The samples are 11 peridotites derived from Marion transform faults, of which 4 are the same as those in Part 1 study (Table 1). In addition to the thin sections made in Part1 study, 7 thin sections were newly made as analytical samples for optical observation and Raman spectroscopy. Thin sections were prepared in the same manner as Part1 study.

2.2. Optical observation and Raman spectroscopy of inclusions

Olivine inclusions were observed by optical microscope with magnification >50 focusing on the size, shape and distribution. To confirm that inclusions were exposed on the surface of the thin section, observations with a reflected light microscopy were also performed.

Raman spectroscopy was performed with Nicolet Almega XR Raman micro-spectrometer (Thermo Fisher Scientific) equipped with a 532 nm Nd-YAG laser, a thermoelectric-cooled charge-coupled detector (256 × 1024 pixels) and an automated confocal microscope (Olympus BX5) housed at the Rock and Mineral Laboratory, Nagoya University. The room temperature was kept at 20 °C. The system was calibrated by 520 cm^{-1} band of Si wafer as a standard at each measurement to check reproducibility of analyses. In the analyses, I chose 43 inclusions from 11 samples that were not exposed on thin section surface to avoid contamination. 100× objective lens (numerical aperture = 0.9) was selected for point analyses to achieve the resolution of 0.6 μm. The acquisition duration was set to 60 seconds with 10 s of exposure time and 6 times of accumulations per point. The range of wavenumber was 106~4233 cm^{-1} so that there is no omission in the detection of peaks.

3. RESULTS

3.1. Description of the inclusions

Coarse olivine grains with diameters of more than several hundred micrometers in the tectonites contained numerous inclusions, while there were few inclusions in fine-grained olivine within matrix of the tectonites and the ultramylonites. Several inclusions were found in porphyroclasts of the ultramylonites, however they were too small to measure. Moreover, minerals other than olivine, such as orthopyroxene (Opx) and clinopyroxene (Cpx), contained almost no inclusions. Olivine grains contain numerous inclusions up to 15μm in diameter with various shapes such as rounded, planar and irregular. The inclusions were continuously distributed, often forming planar structures (Fig. 1). These inclusions were encapsulated with olivine, and distribution of the inclusions and position of serpentine veins and grain boundaries did not seem to be related.

3.2. Compositions of the inclusions

The inclusions in olivine grains contain (1) H_2, (2) low-temperature (LT) serpentine, (3) LT serpentine + H_2, (4) LT serpentine + CH_4, (5) LT serpentine + CH_4 + H_2 and (6) LT serpentine + CH_4 + C (graphite). Inclusions with different compositions existed within the same olivine grain (Table 2). Below, these results are described in detail.

3.2.1. H_2 inclusion

Peaks of Raman spectra were found at ~352, 585cm^{-1} and 4120-4160cm^{-1}, indicating the presence of hydrogen (Fig. 2a). H_2 was detected in 12 inclusions in 6 samples (2 in D17-5, 1 in D19-5, 1 in D19-11, 3 in D19-14, 1 in D19-85 and 4 in D19-8; Table 2).

3.2.2. LT serpentine inclusion

41 inclusions in 9 samples (5 in D17-5, 4 in D19-2, 1 in D19-11, 3 in D19-14, 4 in D19-22, 7 in D19-28, 6 in D19-31, 4 in D19-85 and 7 in D19-86) contained LT serpentine (Table 2). These inclusions exhibited the peaks of Raman spectra at ~690, 960 cm^{-1} and ~3680-3690 cm^{-1}, which is characteristic of hydrous mineral (Fig. 2b). These peaks coincided with those of LT serpentine, indicating that serpentine mineral exists not only as veins but also inclusions.

3.2.3. LT serpentine + H_2 + CH_4 inclusion

There were inclusions exhibiting peaks of Raman spectra at 2911cm^{-1} and ~3060-3070cm^{-1}, which were coincided with those of CH_4 (Fig. 2e). These peaks were detected in 11 inclusions in 5 samples (4 in D17-5, 1 in D19-14, 4 in D19-31, 1 in D19-46 and 1 in D19-8; Table 2). There were no inclusions of CH_4 only, and they coexisted with H_2 and/or LT serpentine mineral.

3.2.4. LT serpentine + CH_4 + C (graphite) inclusion

4 inclusions in 2 samples (3 in D19-31 and 1 in D19-46; Table 2) showed peaks of Raman spectra at 1348, 1580, 2698cm^{-1} and 3242cm^{-1}, indicating the existence of C (graphite) other than LT serpentine mineral and CH_4 (Fig. 2f). Both inclusions contained not only graphite, but also CH_4 and/or LT serpentine mineral.

4. DISCUSSION

4.1. Compositions of the inclusions

The compositions of inclusions are: (1) H_2, (2) LT serpentine, (3) LT serpentine + H_2, (4) LT serpentine + CH_4, (5) LT serpentine + CH_4 + H_2 and (6) LT serpentine + CH_4 + C (graphite). There were inclusions containing only H_2 or LT serpentine, while CH_4 and graphite coexisted with H_2 and/or LT serpentine.

4.1.1. H_2 + CH_4 inclusion

H_2 and CH_4 were detected in 12 and 11 of 43 inclusions, respectively. Furthermore, there were 4 inclusions containing both H_2 and CH_4 (Table 2). It is known that H_2 is generated when olivine reacts with water to form serpentine minerals (reaction (1); e.g., Proskurowski et al., 2008):

$$\underset{\text{olivine}}{9Mg_2SiO_4 + 3Fe_2SiO_4} + 14H_2O = \underset{\text{lizardite}}{6Mg_3Si_2O_5(OH)_4} + \underset{\text{magnetite}}{2Fe_3O_4} + 2H_2 \tag{1}$$

Additionally, CH_4 is generated by next reactions: (2) reduction of CO_2 or (3) olivine, water and CO_2 (e.g. Kelley et al., 2001; Früh-Green et al., 2003; Song et al., 2009):

$$CO_2 + 4H_2 = CH_4 + 2H_2O \tag{2}$$

$$\underset{\text{fayalite}}{24Fe_2SiO_4} + 26H_2O + CO_2 = \underset{\text{lizardite}}{12Fe_3Si_2O_5(OH)_4} + \underset{\text{magnetite}}{4Fe_3O_4} + CH_4 \tag{3}$$

Reactions (1) and (3) of serpentinization with occurrence of H_2 and CH_4 are consistent with their coexistence in inclusions.

4.1.2. Graphite inclusion

There were also a few inclusions including graphite. Graphite is generated by next reactions: (4) CO_2 and CH_4, or (5) olivine, water and CO_2 (Kelley, 1996):

$$CO_2 + CH_4 = 2C + 2H_2O \tag{4}$$

$$\begin{aligned} \underset{\text{olivine}}{27Mg_2SiO_4 + 9\,Fe_2SiO_4} + 38H_2O + 2CO_2 &= \underset{\text{magnetite}}{6Fe_3O_4} + \underset{\text{lizardite}}{18Mg_3Si_2O_5(OH)_4} \\ &\quad + CH_4 + \underset{\text{graphite}}{C} \end{aligned} \tag{5}$$

The reactions (2)~(5) involve CO_2 consumed to generate CH_4 and graphite. Lack of CO_2 is thought to be due to the consumption in the occurrence of CH_4 and graphite. Furthermore, CO_2 and a part of generated CH_4 may have been consumed by the formation of graphite.

4.2. Formation of inclusions

4.2.1. How to crack olivine?

Planar structures of inclusions in coarse olivine grains (Fig. 1). Similar textures have been observed within olivine in peridotites obtained from Oman ophiolite (Miura et al., 2011), Gakkel Ridge, Mid-Atlantic Ridge, Mariana Forearc and East Pacific Rise (Klein et al., 2019) other than SWIR. These planar structures require crack opening to be formed. There are several discussions presented for crack opening mechanisms, the main theories are (1) hydro fracturing due to high fluid pressure (e.g., Précigout et al., 2017) and (2) temporal increase in differential stress and strain rate due to seismicity (e.g., Klein et al., 2019; Kohli and Warren, 2020).

Précigout et al. (2017) found cracked spinel grain filled with amphibole and olivine in peridotitic mylonite and concluded that the cracks had been formed by high fluid pressure based on the mechanics of hydoraulic fracturing (Hubbert and Willis, 1957). One of their spinel cracks is filled with amphibole, while the others are filled with olivine. If fluid pressure really cracked spinel, fluid pressure should have been high around the spinel grain, and other cracks also should have been filled with some hydrous mineral, not olivine. Even if the fluid pressure is high, it appears to be easier for fluid to go through grain boundaries where the material boundaries providing paths than crack and go into mineral grains. Moreover, magnitude of fluid pressure needed to open crack and brittle strength of peridoditic minerals like olivine and spinel have not been provided. The Hubbert and Willis' theory explains crack direction related to principal stress and fluid pressure needed to open cracks in rocks, and not for mineral grain themselves. Therefore, it is not clear that fluid pressure achievable in the upper mantle environment can indeed crack minerals. As a matter of fact, the theory that fluid pressure cracks minerals is not sufficiently verified.

Temporal increments of differential stress and strain rate by seismic activities can explain how to crack minerals (Klein et al., 2019; Kohli and Warren, 2020). It is known that rocks including mantle peridotite undergo ductile deformation at low strain rate under high temperature, however, transition to brittle deformation at high strain rate even in the plastic regime. Chatzaras et al., 2020 found fine-grained microdeformation zones between coarse grains and concluded that the microdeformation zones had been formed by brittle failure and rupture propagation downward to the upper mantle during coseismic event or early postseismic term. Critical strain rate $\dot{\varepsilon_c}$ at which transition from ductile to brittle deformation occurs is provided by Ohuchi et al. (2018):

$$\dot{\varepsilon_c} = \frac{h\rho C_p \kappa R T^2}{\sigma H^* L^2}$$

where, h is the work hardening coefficient (=1), ρ is density (=3.4 g/cm3), C_p is the specific heat (=817 J/kg*K), κ is thermal diffusivity (=0.7 mm^2/s), H^* is the activation enthalpy for deformation (H^*=554 kJ/mol) and L is the size of the sample (grain size in this study for brittle strength of olivine; ~several millimeter). The diameters of grains which containing inclusions ranged from hundreds of micrometers to several millimeters, so that the values of obtained differential stress were ~2-40 MPa based on the piezometer of Van der Wal et al. (1993). At brittle-ductile transition temperature around ~600 °C, $\dot{\varepsilon_c}$ is ~10^{-2}-10^{1} s^{-1} (Fig. 3). The expected strain rate at the moment of earthquake is ~10^{-2}-10^{1} s^{-1} (Kelemen and Hirth, 2007), thus olivine grain can be cracked by temporal increase in strain rate. As a result, planar structure of inclusions is remained in the host mineral. Yet, seismic activities along transform faults are limited within the areas of <600 °C and rapture propagation is canceled by viscous relaxation, this mechanism appears to work only near brittle-ductile transition zone.

Another possible mechanism is Stroh crack mechanism (Stroh, 1954). This mechanism explains crack opening by stress concentration around an obstacle and dense dislocations. If there is an obstacle on the dislocation slip plane, dislocations get stuck and dislocation pile-up occurs around obstacle. Then stress concentrates because dislocation cannot move and deformation is prevented locally. Finally, minerals are crack when they can no longer withstand the concentrated stress. This phenomenon has been observed experimentally in metals (e.g., Tamayo-Meza et al., 2010) and minerals (Gaboriaud et al., 1981 for olivine; Hirth and Tullis, 1994 for quartz; Tullis and Yund, 1987 for feldspar). Especially, Gaboriaud et al. (1981) conducted a series of deformation experiment under the temperature of 20-900 °C, resulting in the formation of cracks within olivine under all temperature conditions. They found that the samples deformed under >600 °C exhibited numerous dislocations around cracks, whereas the samples deformed under <600 °C exhibited no relationship between the formation of cracks and dislocation slip, and concluded that crack opening in ductile regime and brittle-ductile transition were affected by the mobility of dislocation. Figure. 4 shows the formation of inclusions by this mechanism. Stroh crack mechanism needs dislocation mobility and obstacles, and do not depend on stress and strain rate, and dislocation slip can be prevented by impurities, other dislocation when dislocation density is high, grain boundary or inclusion. Based on the necessity of dislocation slip, this mechanism can work under the temperature conditions of >600 °C.

4.2.2. Formation temperature of olivine inclusions

Klein et al. (2019) found fluid inclusions in peridotites derived from SWIR and proposed that water trapped as inclusions in olivine grains above ~400 °C generates CH_4, H_2 and serpentine below ~340 °C. Kohli and Warren (2020) observed planar structures of olivine-hosted fluid inclusions, and suggested that these planar structures of fluid inclusions had been formed by formation and recovery of cracks in olivine grain by temporary change in differential stress due to earthquakes, and earthquakes along the transform faults occur brittle area below the temperature of 600 °C (e.g., Abercrombie and Ekström, 2001; Roland et al., 2010).

In this study, planar structures of the inclusions within olivine grains were observed in coarse olivine grains of the tectonites, which were similar to those observed by Kohli and Warren (2020), while there were few inclusions in fine-grained matrix of the tectonites and the ultramylonites. Grain sizes of olivine in matrix are finer than inclusions especially in the ultramylonites, therefore inclusions in these fine olivine grains seem to have lost by deformation and accompanying grain size reduction. Although LT serpentine existed as inclusions encapsulated with olivine and did not exist as veins. If water infiltrated into cracks of olivine below the temperature of 350 °C, which is the stable condition of LT serpentine, serpentine veins should have been occurred instead of inclusions, so that water appears to have been trapped into olivine cracks at higher temperature than 350 °C, then formed serpentine inclusions. Yet, formation of olivine cracks requires brittle to semi-brittle deformation. The temperature of brittle-ductile transition zone is ~600 °C, which is the lower limit of ductile deformation of olivine. Thus, water seems to have been entrained in olivine grains lower than 600 °C.

4.3. Water infiltration along the transform fault and the formation of olivine inclusions

Most inclusions contained low-temperature serpentine. These serpentine inclusions were contained in also the peridotites in which amphiboles were observed in Part1 study. Additionally, H_2

and CH_4 are also generated in relation to serpentinization, thus water in require for their occurrence based on the reaction (1) to (3). This suggests that water infiltrated to the depth where the temperature is up to ~800 °C, and trapped in olivine grains as inclusions. LT serpentine minerals are stable under ~350 °C, thus water in inclusions seems to have reacted with host olivine to form LT serpentine inclusions. Based on the above, not only the existence on hydrous minerals and olivine CPOs formed under hydrous conditions but also the occurrence of hydrous inclusions can be an evidence of water infiltration along the transform fault. The water that had infiltrated into shallow upper mantle where the temperature is up to ~800 °C was trapped within olivine grains as inclusions, and (1) serpentinization had occurred under ~350 °C, (2) H_2 and CH_4 had been generated. Furthermore, (3) a part of generated CH_4 was consumed to form graphite (Fig. 5).

5. CONCLUSIONS

I analyzed 43 inclusions in 11 peridotites derived from Marion transform fault, SWIR. Coarse olivine grains in the tectonites contained numerous inclusions with rounded, planar and irregular shapes whose sizes were up to ~15 μm. The inclusions were continuously distributed to form planar structures. These inclusions consisted of LT serpentine, H_2 and coexisting CH_4 and graphite. Olivine is weaker and deforms easier than pyroxenes under low temperature condition assumed for the Marion transform fault, therefore inclusions appear to have been formed preferentially in olivine grain. Based on the lack of serpentine veins and brittle to semi-brittle features, it is suggested that the range of formation temperature of inclusions is 350 to 600 °C. LT serpentine inclusions in the peridotites with amphiboles suggests that water infiltrated to the depth where the temperature is up to ~800 °C, and reacted with host olivine to form LT serpentine under ~350 °C. Consequently, in addition to occurrence of hydrous minerals and CPOs of olivine, the hydrous inclusions indicates that water infiltrated into upper mantle from the transform fault.

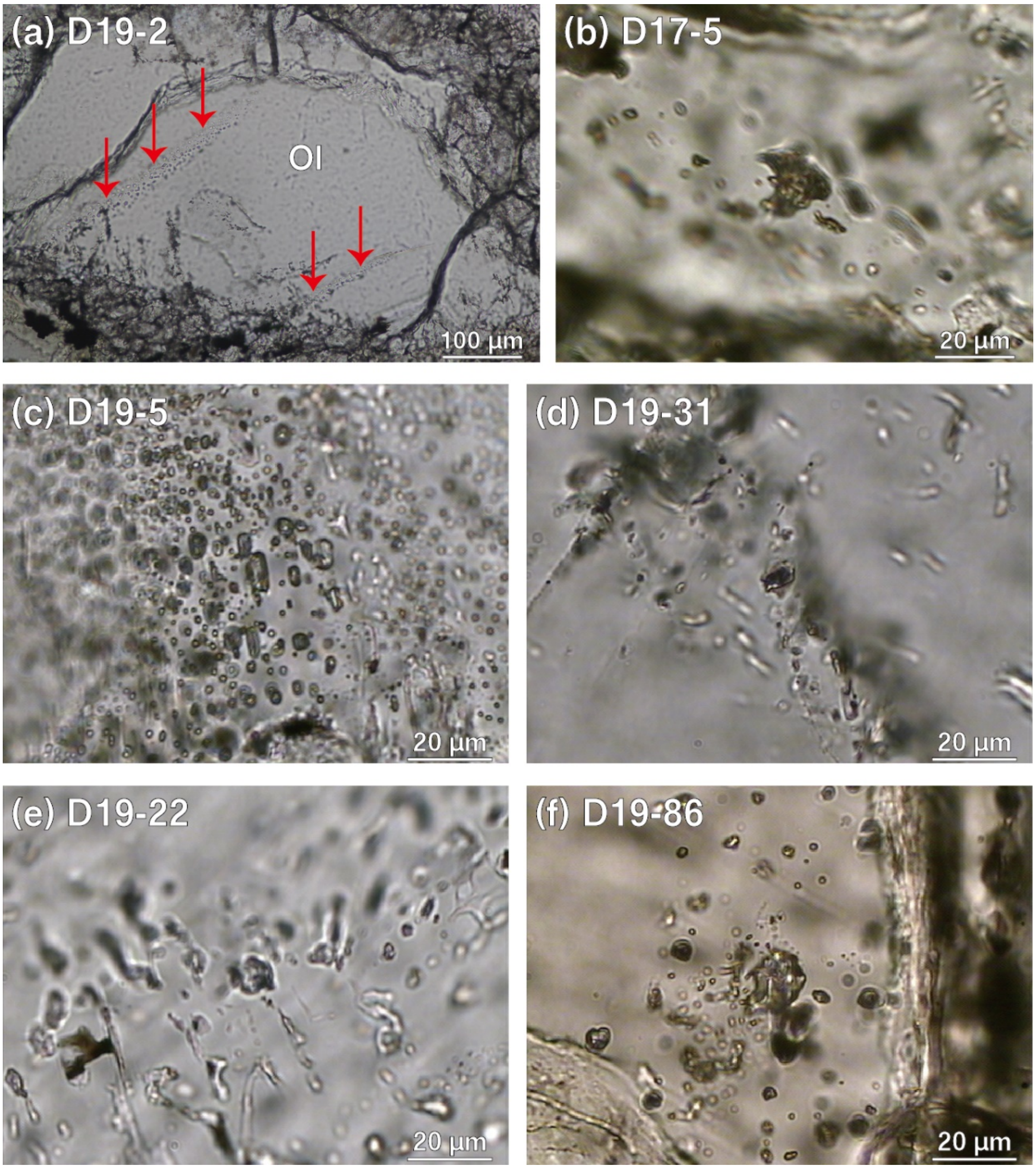

Figure 1. Optical photomicrographs of olivine-hosted inclusions. Red arrows in (a) show location of inclusions. Abbreviation: Ol = olivine

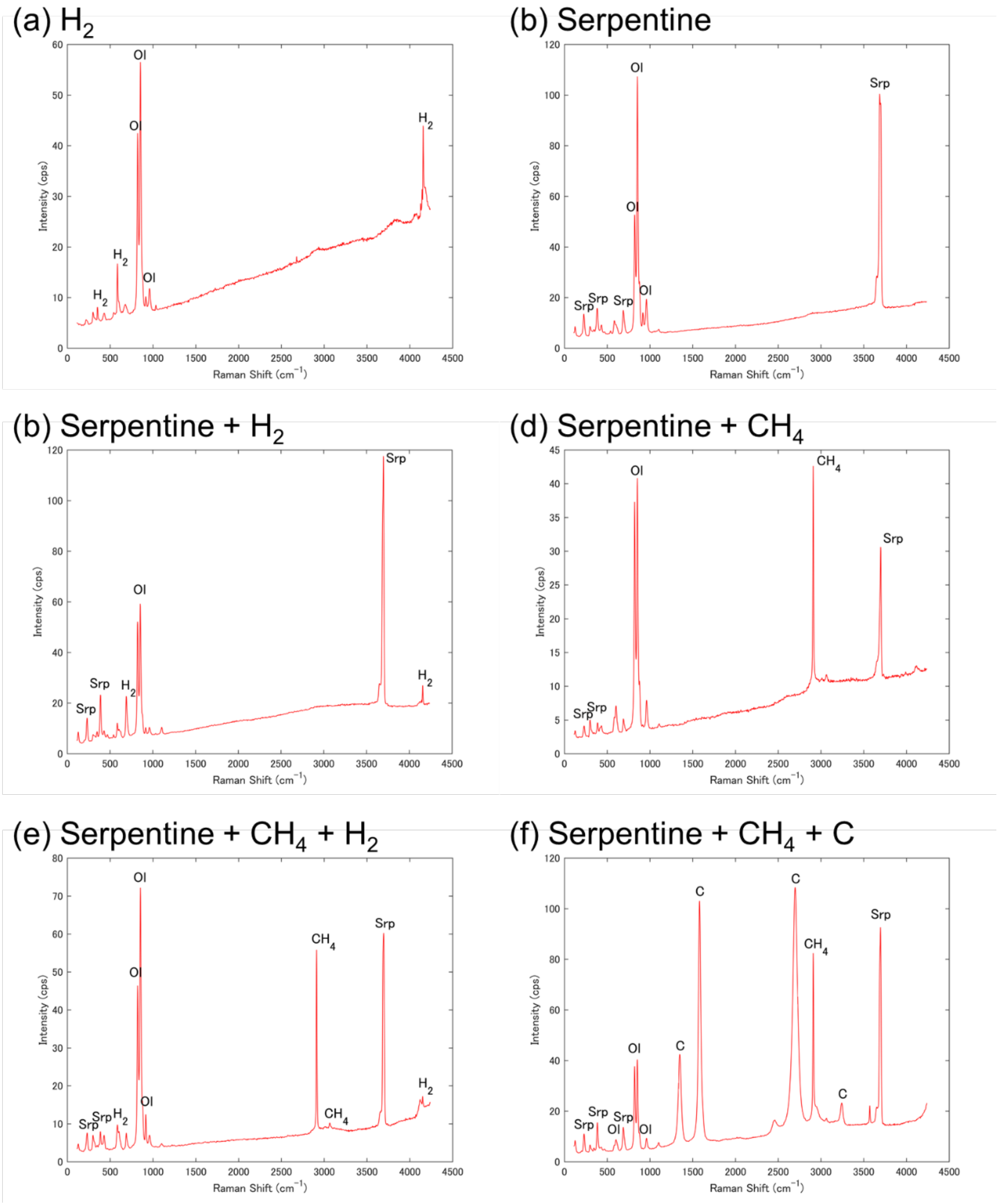

Figure 2. Peaks of Raman spectra of olivine-hosted inclusions. Abbreviations: Srp = serpentine, H_2 = hydrogen, CH_4 = methane, C = graphite

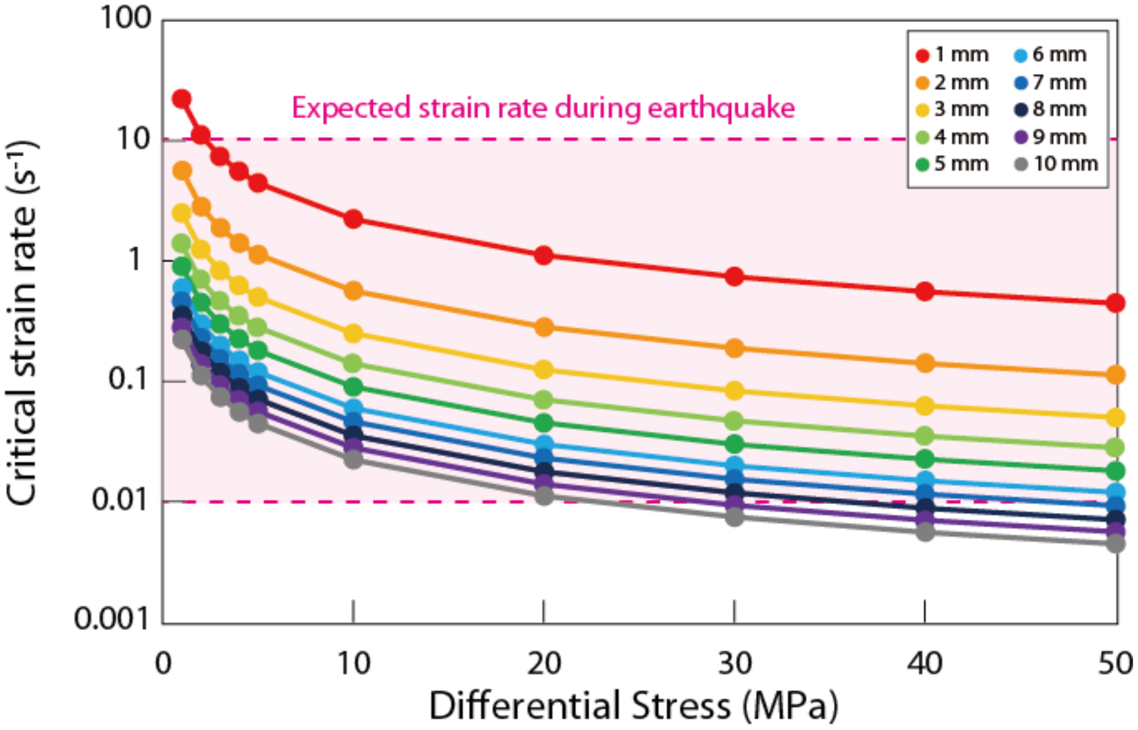

Figure 3. Change in critical strain rate relative to differential stress. Critical strain rate is the strain rate at which the transition from ductile to brittle deformation occurs. Legends are for grain size. Pink area refers to the expected strain rate during earthquake (Kelemen and Hirth, 2007).

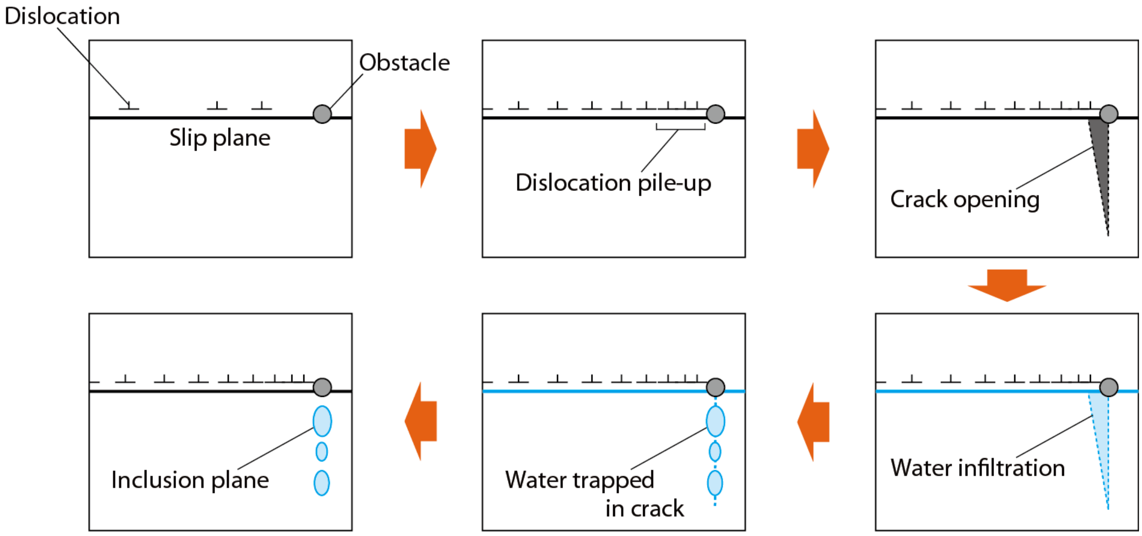

Figure 4. Formation of inclusions by Stroh crack mechanism (Stroh, 1954). An obstacle on the slip plane prevents dislocations from slipping and causes dislocation pile-up. Then, stress is concentrated around the obstacle and dislocation pile-up, resulting in the crack opening. Water goes into cracks and is trapped by healing of the cracks. Finally, planar structure of inclusions is formed.

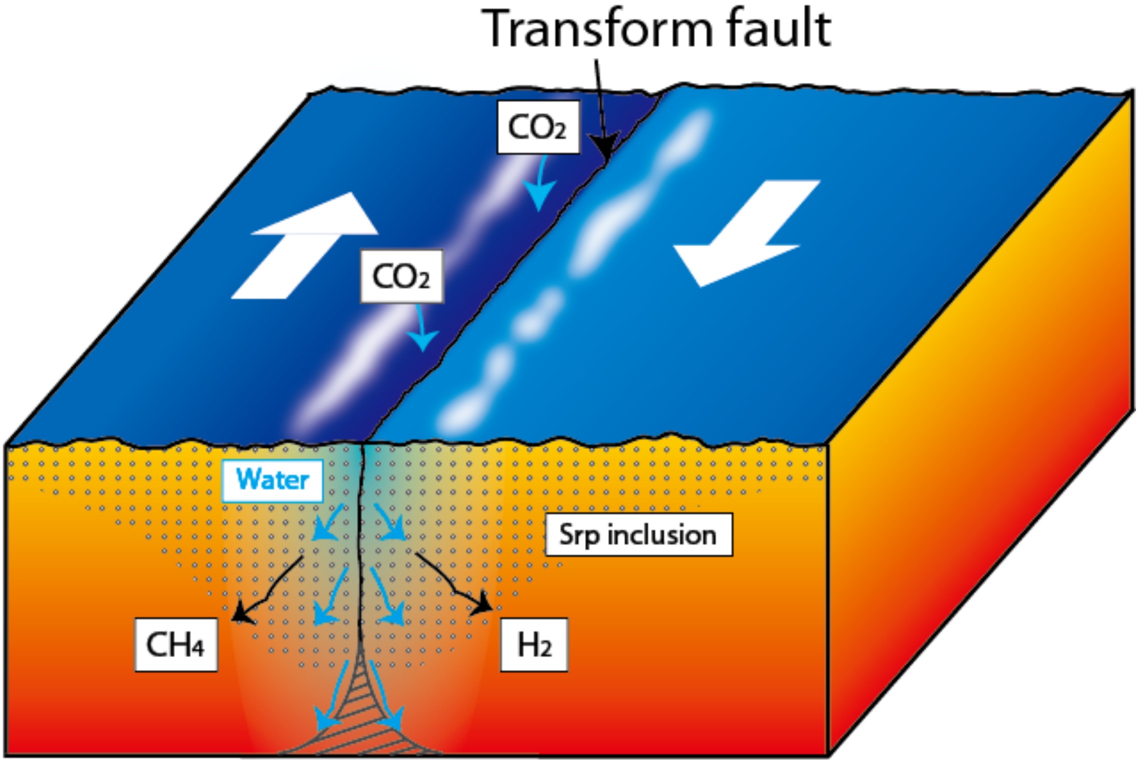

Figure 5. Model of water infiltration and formation of olivine-hosted inclusions along the transform fault. Water infiltrates into shallow part of upper mantle where the temperature in up to ~800 °C and trapped as inclusions in olivine grains. After the temperature dropped, serpentinization occurs and H_2, CH_4 and C are generated by reducing of CO_2 from seawater. Abbreviations: Srp = serpentine, H_2 = hydrogen, CH_4 = methane, CO_2 = carbon dioxide

Table 1. Sampling sites of the peridotites.

Dr	Sample Number	Lat	Lon	Depth (m)	Texture	Location
17	5	-46.378	33.508	2380	Heterogeneous texture	West Wall of Marion Transform fault
19	2	-46.507	33.832	3900	Heterogeneous texture	East Wall of Marion Transform fault
19	5	-46.507	33.832	3900	Heterogeneous texture	East Wall of Marion Transform fault
19	11	-46.507	33.832	3900	Heterogeneous texture	East Wall of Marion Transform fault
19	14	-46.507	33.832	3900	Heterogeneous texture	East Wall of Marion Transform fault
19	22	-46.507	33.832	3900	Heterogeneous texture	East Wall of Marion Transform fault
19	28	-46.507	33.832	3900	Ultramylonite	East Wall of Marion Transform fault
19	31	-46.507	33.832	3900	Ultramylonite	East Wall of Marion Transform fault
19	46	-46.507	33.832	3900	Ultramylonite	East Wall of Marion Transform fault
19	85	-46.507	33.832	3900	Heterogeneous texture	East Wall of Marion Transform fault
19	86	-46.507	33.832	3900	Heterogeneous texture	East Wall of Marion Transform fault

Table 2. Numbers of analysis and compositions of olivine-hosted inclusions. Numbers of Srp, H_2, CH_4 and C are internal numbers. Abbreviations: Srp = serpentine, H_2 = hydrogen, CH_4 = methane

Sample	No. of Analysis	Srp	H_2	CH_4	C (graphite)
D17-5	5	5	2	4	0
D19-2	4	4	0	0	0
D19-5	1	0	1	0	0
D19-11	1	1	1	0	0
D19-14	3	3	3	1	0
D19-22	4	4	0	0	0
D19-28	7	7	0	0	0
D19-31	6	6	0	4	3
D19-46	1	0	0	1	1
D19-85	4	4	1	0	0
D19-86	7	7	4	1	0
Total	43	41	12	11	4

ACKNOWLEDGEMENTS

I really appreciate Prof. Katsuyoshi Michibayashi and his passionate guidance. A/Prof. Yui Koketsu is greatly appreciated as well for provision of insightful comments. Prof. Henry Dick of Woods Hole Oceanographic Institution is thanked for providing the peridotites derived from SWIR. I am grateful for kind help by Shiho Furukawa during my PhD life. I would also like to appreciate all members of the Research Group of Mineralogy and Petrology at Nagoya University for constructive comments and stimulative discussion.

REFERENCES

Abercrombie, R.E., Ekström, G., 2001. Earthquake slip on oceanic transform faults. Nature, 410, 74-77.

Abramson, E.H., Brown, J.M., Slutsky, I.J., Zang, J.J., 1997. The elastic constants of San Carlos olivine to 17 GPa. Journal of Geophysical Research, 102, 12253-12263.

Arai, S., 1994. Characterization of spinel peridotites by olivine-spinel compositional relationships: Review and interpretation. Chemical Geology, 115, 191-204.

Ballhaus, C., Berry, R.F., Green, D.H., 1991. High pressure experimental calibration of the olivine-orthopyroxene-spinel oxygen geobarometer: implications for the oxidation state of the upper mantle. Contributions to Mineralogy and Petrology, 107(1), 27-40.

Brey, G.P., Köhler, T., 1990. Geothermobarometry in four-phase Lherzolites II. New thermobarometers, and practical assessment of existing thermobarometers. Journal of Petrology, 31(6), 1353–1378.

Chatzaras, V., Tikoff, B., Kruckenberg, S.C., Titus, S.J., Teyssier, C., Drury, M.R., 2020. Stress variations in space and time within the mantle section of an oceanic transform zone: Evidence for the seismic cycle. Geology, 48(6), 569-573.

Czertowicz, T.A., Toy, V.G., Scott, J.M., 2016. Recrystallisation, Phase mixing and strain localisation in peridotite during rapid extrusion of sub-arc mantle lithosphere. Journal of Structural Geology, 88, 1-19.

Dick, H.J.B., Bullen, T., 1984. Chromian spinel as a petrogenetic indicator in abyssal and alpine-type peridotites and spatially associated lavas. Contributions to Mineralogy and Petrology, 86, 54-76.

Dick, H.J.B., 1989, Abyssal peridotites, very slow spreading ridges and ocean ridge magmatism. In: Saunderes, A. D. and Norry, M. J. (Eds), Geological Society of London, Special Publication, pp. 71-105.

Dick, H.J.B., Lin, J., Schouten, H., 2003. An ultraslow-spreading class of ocean ridge. Nature, 426, 405-412.

Dick, H.J.B., Tivey, M.A., Tucholke, B.E., 2008. Plutonic foundation of a slow-spreading ridge segment: Oceanic core complex at Kane Megamullion, 23 degrees 30 ' N, 45 degrees 20 ' W.

Geochemistry Geophysics Geosystems, 9.

Dick, H.J.B., MacLeod, C.J., Blum, P., Abe, N., Blackman, D.K., Bowles, J.A., Cheadle, M.J., Cho, K., Ciazela, J., Deans, J.R., Edgcomb, V.P., Ferrando, C., France, L., Ghosh, B., Ildefonse, B., John, B., Kendrick, M.A., Koepke, J., Leong, J.A.M., Liu, C., Ma, Q., Morishita, T., Morris, A., Natland, J.H., Nozaka, T., Pluemper, O., Sanfilippo, A., Sylvan, J.B., Tivey, M.A., Tribuzio, R., Viegas, G., 2019. Dynamic Accretion Beneath a Slow-Spreading RidgeSegment: IODP Hole 1473A and the Atlantis BankOceanic Core Complex. Journal of Geophysical Research: Solid Earth, 124, 12631-12659.

Francis, T.J.G., 1981. Serpentinization faults and their role in the tectonics of slow spreading ridges. Journal of Geophysical Research, 86, 616-622.

Früh-Green, G.L., Kelley, D.S., Bernasconi, S.M., Karson, J.A., Ludwig, K.A., Butterfield, D. A., Boschi, A., Proskurowski, G., 2003. 30,000 Years of Hydrothermal Activity at the Lost City Vent Field. Science, 301(5632), 495-498.

Gaboriaud, R.J., Darot, M., Gueguen, Y., Woirgard, J., 1981. Dislocations in olivine indented at low temperatures. Physics and Chemistry of Minerals, 7(2), 100-104.

Gerya, T.V., Connolly, J.A.D., Yuen, D.A., 2008. Why is terrestrial subduction one-sided? Geology, 36, 43-46.

Hall, C.E., Gurnis, M., Sdrolias, M., Lavier, L.L., Müller, R.D., 2003. Catastrophic initiation of subduction following forced convergence across fracture zones. Earth and Planetary Science Letters, 212, 15-30.

Hatakeyama, K., Katayama, I., Hirauchi, K., Michibayashi, K., 2017. Mantle hydration along outer-rise faults inferred from serpentinite permeability. Scientific Reports, 7, http://dx.doi.org/10.1038/s41598-017-14309-9.

Hidas, K., Tommasi, A., Garrido, C.J., Padrón-Navarta, J.A., Mainprice, D., Vauchez, A., Barou, F., Marchesi, C., 2016. Fluid-assisted strain localization in the shallow subcontinental lithospheric mantle. Lithos, 262, 636-650.

Hirauchi, K., Fukushima, K., Kido, M., Muto, J., Okamoto, A., 2016. Reaction-induced rheological weakening enables oceanic plate subduction. Nature Communications, 7, http://dx.doi.org/10.1038/ncomms12550.

Hirth, G., Tullis, J., 1994. The brittle-plastic transition in experimentally deformed quartz aggregates. Journal of Geophysical Research: Solid Earth, 99, 11731-11747.

Holland, T., Blundy, J., 1994. Non-ideal interactions in calcic amphiboles and their bearing on amphibole-plagioclase thermometry. Contributions to mineralogy and petrology, 116(4), 433-447.

Hubbert, M.K., Willis, D.G., 1957. Mechanics of hydraulic fracturing. Transactions of the AIME, 210, 153-168.

Jaroslow, G.E., Hirth, G., Dick, H.J.B., 1996. Abyssal peridotite mylonites: implications for grain-size sensitive flow and strain localization in the oceanic lithosphere. Tectonophysics, 256, 17-37.

Jenkins, D.M., 1981. Experimental phase relations of hydrous peridotites modelled in the system H_2O-CaO-MgO-Al_2O_3-SiO_2. Contributions to Mineralogy and Petrology, 77, 166-176.

Johanesen, K.E., Platt, J.P., 2015. Rheology, microstructure, and fabric in a large scale mantle shear zone, Ronda Peridotite, southern Spain. Journal of Structural Geology, 73, 1-17.

Jung, H., Karato, S., 2001. Water-Induced Fabric Transitions in Olivine. Science, 293, 1460-1463.

Kakihata, Y., Michibayashi, K., Dick, H.J.B., 2022. Heterogeneity in texture and crystal fabric of intensely hydrated ultramylonitic peridotites along a transform fault, Southwest Indian Ridge. Tectonophysics, 823, 229206.

Karato, S., Jung, H., 2003. Effects of pressure on high-temperature dislocation creep in olivine. Philosophical Magazine, 83, 401-414.

Karato, S., Jung, H., Katayama, I., Skemer, P., 2008. Geodynamic Significance of Seismic Anisotropy of the Upper Mantle: New Insights from Laboratory Studies. Annual Review of Earth and Planetary Sciences, 36, 59-95.

Katayama, I., Jung, H., Karato, S., 2004. New type of olivine fabric from deformation experiments at modest water content and low stress. Geology, 32, 1045-1048.

Kelemen, P.B., Hirth, G., 2007. A periodic shear-heating mechanism for intermediate-depth earthquakes in the mantle. Nature, 446, 787-790.

Kelley, D.S., 1996. Methane-rich fluids in the oceanic crust. Journal of Geophysical Research, 101(B2), 2943-2962.

Kelley, D.S., Karson, J.A., Blackman, D.K., Früh-Green, G.L., Butterfield, D.A., Lilley, M.D., Olson, E.J., Schrenk, M.O., Roe,K.K., Lebon, G.T., Rivizzigno, P., the AT3-60 Shipboard Party,2001. An off-axis hydrothermal vent field near the Mid-Atlantic Ridge at 30° N. Nature, 412, 145-149.

Kerric, D., 2002. Serpentinite Seduction. Science, 298, 1345-1346.

Klein, F., Grozeva, N.G., Seewald, J., 2019. Abiotic methane synthesis and serpentinization in olivine-hosted fluid inclusions. Proceedings of the National Academy of Sciences, 116, 17666–17672.

Kohli, A.H., Warren, J.M., 2020. Evidence for a Deep Hydrologic Cycle on Oceanic Transform Faults. Journal of Geophysical Research: Solid Earth, 125, e2019JB017751.

Korenaga, J., 2007. Thermal cracking and the deep hydration of oceanic lithosphere: A key to the generation of plate tectonics? Journal of Geophysical Research, 112, 1-20.

Korenaga, J., 2010. On the likelihood of plate tectonics on super-Earths: Does size matter? The Astrophysical Journal Letters, 725, 43-36.

Korenaga, J., 2013. Initiation and Evolution of Plate Tectonics on Earth: Theories and Observations. Annual Review of Earth and Planetary Sciences, 41, 117-151.

Michibayashi, K., Oohara, T., 2013. Olivine fabric evolution in a hydrated ductile shear zone at the Moho Transition Zone, Oman Ophiolite. Earth and Planetary Science Letters, 377-378, 299-310.

Michibayashi. K., 2015. Olivine Crystallographic Fabrics and Their P-wave Velocity Structures within Peridotites in the Uppermost Mantle. Journal of Geography (Chigaku Zasshi), 124, 397-409.

Michibayashi, K., Mainprice, D., Fujii, A., Uehara, S., Shinkai, Y., Kondo, Y., Ohara, Y., Ishii, T., Fryer, P., Bloomer, S.H., Ishiwatari, A., Hawkins, J.W., Ji, S., 2016. Natural olivine crystal-fabrics in the western Pacific convergence region: A new method to identify fabric type. Earth and Planetary Science Letters, 443, 70-80.

Miura, M., Arai, S., Mizukami, T., 2011. Raman spectroscopy of hydrous inclusions in olivine and orthopyroxene in ophiolitic harzburgite: implications for elementary processes in serpentinization. Journal of Mineralogical and Petrological Sciences, 1103030170-1103030170.

Kohli, A.H., Warren, J.M., 2020. Evidence for a deep hydrologic cycle on oceanic transform faults. Journal of Geophysical Research, 125(2), e2019JB017751, https://doi.org/10.1029/2019jb017751.

Mainprice, D., Silver, P.G., 1993. Interpretation of SKS waves using samples from the subcontinental lithosphere. Physics of Earth and Planetary Interior, 78, 257-280.

Ohuchi, T., Lei, X., Higo, Y., Tange, Y., Sakai, T., Fujino, K., 2018. Semi-brittle behavior of wet olivine aggregates: the role of aqueous fluid in faulting at upper mantle pressures. Contributions to Mineralogy and Petrology, 173(10), 1-21.

Peacock, S.M., 2001. Are the lower planes of double seismic zones caused by serpentine dehydration in subducting oceanic mantle? Geology. 29, 299-302.

Précigout, J., Prigent, C. Palasse, L., Pochon, A., 2017. Water pumping in mantle shear zones. Nature Communications, 8, http://dx.doi.org/10.1038/ncomms15736.

Prigent, C., Warren, J.M., Kohli, A.H., Teyssier, C., 2020. Fracture-mediated deep seawater flow and mantle hydration on oceanic transform faults. Earth and Planetary Science Letters, 532, 115988.

Proskurowski, G., Lilley, M.D., Seewald, J.S., Früh-Green, G.L., Olson, E.J., Lupton, J.E., Sylva, S.P. and Kelly, D.S., 2008. Abiogenic hydrocarbon production at Lost City Hydrothermal field. Science, 319, 604-607.

Roland, E., Behn, M.D., Hirth, G., 2010. Thermal-mechanical behavior of oceanic transform faults: Implications for the spatial distribution of seismicity. Geochemistry, Geophysics, Geosystems, 11, http://dx.doi.org/10.1029/2010GC003034.

Sauter, D., Mendel, V., Rommevaux-Jestin, C., Parson, L.M., Fujimoto, H., Mével, C., Cannat, M., Tamaki, K., 2004. Focused magmatism versus amagmatic spreading along the ultra-slow spreading Southwest Indian Ridge: Evidence from TOBI side scan sonar imagery. Geochemistry, Geophysics, Geosystems, 10, http://dx.doi.org/10.1029/2004GC000738.

Sauter, D., Cannat, M., Rouméjon, S., Andreani, M., Brot, D., Bronner, A., Brunelli, D., Carlut, J., Delacour, A., Guyader, V., MacLeod, C.J., Manatschal, G., Mendel, V., Ménez, B., Pasini, V., Ruellan, E., Searle, R., 2013. Continuous exhumation of mantle-derived rocks at the Southwest Indian Ridge for 11 million years. Nature Geoscience, 6, 314-320.

Seyler, M., Cannat, M., Mével, C., 2003. Evidence for major-element heterogeneity in the mantle source of abyssal peridotites from the Southwest Indian Ridge (52° to 68°E). Geochemistry, Geophysics, Geosystems, 4, http://dx.doi.org/10.1029/2002GC000305.

Schlindwein, V., Schmid, F., 2016. Mid-ocean-ridge seismicity reveals extreme types of ocean lithosphere. Nature, 535, 276-279.

Sclater, J.G., Grindlay, N.R., Madsen, J.A., Rommevaux-Jestin, C., 2005. Tectonic interpretation of the Andrew Bain transform fault: Southwest Indian Ocean. Geochemistry, Geophysics, Geosystems, 6, http://dx.doi.org/10.1029/2005GC000951.

Skemer, P., Warren, J.M., Kelemen, P.B., Hirth, G., 2009. Microstructural and rheological evolution of a mantle shear zone. Journal of Petrology, 51, 43-53.

Song, S., Su, L., Niu, Y., Lai, Y., Zhang, L., 2009. CH_4 inclusions in orogenic harzburgite: Evidence for reduced slab fluids and implication for redox melting in mantle wedge. Geochimica et Cosmochimica Acta, 73(6), 1737-1754.

Soustelle, V., Manthilake, G., 2017. Deformation of olivine-orthopyroxene aggregates at high pressure and temperature: Implications for the seismic properties of the asthenosphere. Tectonophysics, 694, 385-399.

Stern, R.J., 2004. Subduction initiation: Spontaneous and induced. Earth and Planetary Science Letters, 226, 275-292.

Stipp, M., Stünitz, H., Heilbronner, R., Schmid, S.M. 2002. The eastern Tonale fault zone: a ‘natural laboratory’ for crystal plastic deformation of quartz over a temperature range from 250 to 700 °C. Journal of Structural Geology, 24, 1861-1884.

Stroh, A.N., 1954. The formation of cracks as a result of plastic flow. Proceedings of the Royal Society of London. Series A. Mathematical and Physical Sciences, 223, 404-414.

Ulmer, P., Trommsdorf, V., 1995. Serpentinite stability to mantle depths to subduction-related magmatism. Science. 268, 858-861.

Tamayo-Meza, P.A., Yermishkin, V., Schabes-Retchkiman, P., 2010. The effect of crystal geometry on the formation and crack development in molybdenum single crystals. Journal of Applied Physics, 107(7), 073503.

Tasaka, M., Zimmerman, M.E., Kohlstedt, D.L., 2016. Evolution of the rheological and microstructural properties of olivine aggregates during dislocation creep under hydrous conditions. Journal of Geophysical Research, 121, 92–113.

Taylor, W.R., 1998. An experimental test of some geothermometer and geobarometer formulations for upper mantle peridotites with application to the thermobarometry of fertile lherzolite and garnet websterite. Neues Jahrbuch für Geologie und Paläontologie Abhandlugen, 172(2-3), 381–408.

Tucholke, B.E., Lin, J., 2004. A geological model for the structure of rdige segments in slow spreading ocean crust. Journal of Geophysical Research, 99, 11937 - 11958.

Tullis, J., Yund, R.A., 1987. Transition from cataclastic flow to dislocation creep of feldspar: Mechanisms and microstructures. Geology, 15(7), 606-609.

Van der Wal, D., Chopra, P., Drury, M., Gerald, J.F., 1993. Relationships between dynamically recrystallized grain size and deformation conditions in experimentally deformed olivine rocks. Geophysical Research Letters, 20(14), 1479-1482.

Warren, J.M., Hirth, G., 2006. Grain size sensitive deformation mechanisms in naturally deformed peridotites. Earth and Planetary Science Letters, 248(1-2), 438-450.

Witt-Eickschen, G., Seck, H.A., 1991. Solubility of Ca and Al in orthopyroxene from spinel peridotite: an improved version of an empirical geothermometer. Contributions to Mineralogy and Petrology, 106(4), 431–439.

Zhou, H., Dick, H.J.B., 2013. Thin crust as evidence for depleted mantle supporting the Marion Rise. Nature, 494, 195-200.